UNIVERSITÀ POLITECNICA DELLE MARCHE
FACOLTÀ DI INGEGNERIA
Dipartimento di Ingegneria dell'Informazione

Master's degree in BIOMEDICAL ENGINEERING

FDTD analysis of Reconfigurable intelligent surfaces for 5G applications in presence of the human body

Supervisor:

Prof. Valter MARIANI PRIMIANI

Author:
Riccardo FREDDARA

Co-supervisor:
Prof. Franco MOGLIE

A.A. 2021/2022

INDEX

ABSTRACT

Everywhere in the environment, electromagnetic fields can be produced by either natural or man-made sources and are absolutely invisible to the human eye.

Since more and more artificial sources have been produced as a result of rising electricity demand, ever-improving technology, and changes in social behavior, electromagnetic field exposure has been constantly rising. Both at home and at work, everyone is exposed to a complex mixture of weak electric and magnetic fields due to the production and transmission of energy, home and office appliances, industrial machinery, telecommunications, and broadcasting.

The primary biological impact of electromagnetic and radiofrequency radiation is heating. This fact is used in microwave ovens to warm meals. People are typically exposed to radiofrequency fields at levels that are substantially lower than what is required to cause considerable heating. The fundamental element of current rules is the heating impact of radio waves. Researchers are also looking into the idea that prolonged exposure could have effects below the threshold for body heating. Although low level, prolonged exposure to radiofrequency or power frequency fields has not yet been linked to any known harmful health effects, researchers are still actively investigating this topic. Metasurfaces are next-generation engineered devices that are still almost completely unknown but have almost unlimited potential.

In fact, these devices were initially created for the purpose of redirecting a more precise signal to those areas that are difficult to reach due to a particularly adverse environment full of obstacles.

In fact, the metasurfaces are capable, through a precise configuration of the elements that constitute it, of focusing the electromagnetic signal at a precise point in space, this ensures an improved operation of the devices that constitute the environment, but is not enough, a future possibility of use could be to exploit the metasurface to limit electromagnetic exposure by human tissues.

This could be possible due to the fact that a possible smart reconfigurable metasurface would be able to track and geolocate the devices that are in contact with humans in the everyday life and thus be able to focus the signal received from the source much more precisely on the device so as not only to make it work more efficiently but also to precisely reduce the electromagnetic exposure of tissues.

The purpose of this study is to develop through the numerical analysis method FDTD implemented in C programming language a metasurface model composed of varactor diodes at different capacitances, which can be configured manually, and to evaluate the electric field distributions on it as a result of the 'incidence of a plane wave, also the reflection of the signal passing through the metasurface at a generic point in space is evaluated.

Then the metasurface will be placed in an environment with a biological tissue, a device, a PEC barrier, and a dipole antenna. The purpose is to carry out a series of simulations to demonstrate that the presence of the metasurface is capable of causing a lower absorption of the reflected signal by tissues

1. INTRODUCTION

1.1 METAMATERIALS

One of the most fascinating areas of research in nanotechnologies right now is metamaterials. These materials have attracted worldwide attention from a variety of perspectives because the electromagnetic properties that can be obtained with them are nonexistent in nature. In the last twenty years, some of the phenomena that have been explored only theoretically, like invisibility, the negative refraction and superlenses have been widely shown in different systems. However, there are still numerous unexplored pathways, all of them equally fascinating and potentially revolutionary. From this point of view, the only restriction appears to be our capacity to imagine innovative geometries, new phenomena, and so new metamaterials.

The electromagnetic properties of a material, for example, are generally dependent on two factors: the chemical characteristics of the individual atoms that build up the material and the way in which these are ordered in space.

Metamaterials, artificially produced in the laboratory, are composed of elementary cells that take the place of molecules and atoms of traditional materials. Their geometry and order in space make them able to modify the interaction with electromagnetic waves, from microwaves to the visible and infrared, providing them unique characteristics [1].

The electromagnetic properties of materials are described, through the use of Maxwell's equations, from two fundamental quantities: electrical permittivity ε and the magnetic permeability μ. These are specific quantities of materials and are, in general, tensor quantities. From the physical point of view, permittivity describes how the electric field and the material interact, or how much the material is polarized when it interacts with an electric field. The characteristics are also valid for permeability, where the field of interaction, however, is the magnetic one:

$$\mathbf{P} = \varepsilon_0 (\varepsilon_r - 1) \mathbf{E}$$

$$\mathbf{M} = (\mu_r - 1) \mathbf{H} \tag{1.1}$$

Where P and M are respectively the dielectric and magnetic polarizability, while E and H are the fields electric and magnetic, ε_0 and μ_0 and ε_r and μr are the permittivity and permeability of vacuum and those relative of the medium, respectively. By simplifying with respect to the vacuum constants, the characteristic quantities of the materials are defined

$$\varepsilon = \varepsilon_0 \varepsilon r \text{ and } \mu = \mu_0 \mu r. \tag{1.2}$$

From a macroscopic point of view it is possible to subdivide all materials existing in nature on the basis of the values of ε and μ, as shown in Fig. 1.

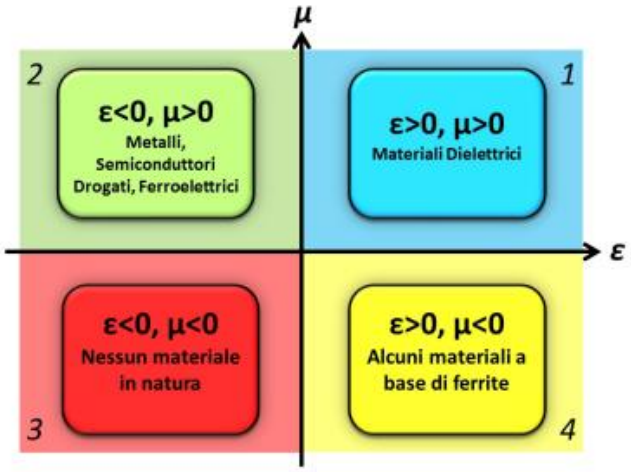

Fig.1 Division of all materials existing in nature in base of their permittivity and permeability

In region 1 are located materials with ε and μ both positive, this region corresponds to the most common cases, and many dielectric materials are part of it. In the second quadrant there are materials that have negative permittivity. This is used to happen in

metals, in semiconductors doped and in ferroelectric materials, at least in certain wavelength ranges, all below the so-called plasma frequency.
Region 4 includes some base materials of ferrite which offer negative permeabilities, but whose magnetic behavior decays beyond microwave range.
The third quadrant includes those materials which simultaneously offer negative permittivity and permeability, and it is, on the contrary of the others, completely empty: substances with this type of characteristics are not present in nature [1].

Maybe because of their curious non-existence, the materials of the third quadrant have attracted interest, at first theoretical, to predict and evaluate their possible electromagnetic properties. In 1968, in fact, he was the Russian theoretical physicist Victor Veselago to analyze its possible characteristics. Let's consider, for example, what happens when a monochromatic plane wave propagates in a third quadrant medium. In general, the electrical and magnetic components of the wave can be written as:

$$\mathbf{E}(\omega,\mathbf{k}) = \mathbf{E_0} \cdot e^{i\mathbf{k}\cdot\mathbf{r} - i\omega t}$$
$$\mathbf{H}(\omega,\mathbf{k}) = \mathbf{H_0} \cdot e^{i\mathbf{k}\cdot\mathbf{r} - i\omega t} \quad (1.3)$$

where **ω** is the frequency and **k** the wave vector.
Maxwell's equations, in local form, are:

$$\nabla \cdot \mathbf{B} = 0, \qquad \nabla \cdot \mathbf{D} = \rho$$
$$\nabla \times \mathbf{H} = \mathbf{J} + \frac{\partial \mathbf{D}}{\partial t}, \qquad \nabla \times \mathbf{E} = -\frac{\partial \mathbf{B}}{\partial t} \quad (1.4)$$

Where

$$\mathbf{D} = \varepsilon \mathbf{E} = \varepsilon_0 \varepsilon_r \mathbf{E} \text{ e } \mathbf{B} = \mu \mathbf{H} = \mu_0 \mu_r \mathbf{H} \quad (1.5)$$

are the fields of electric and magnetic induction, respectively. If we consider the case in which neither free charges (ρ) or currents are present (J), the equations are simplified:

$$\nabla \times \left(\mathbf{E_0} \cdot e^{i\mathbf{k}\cdot\mathbf{r}-i\omega t}\right) = -\frac{\partial}{\partial t}\left(\mu \cdot \mathbf{H_0} \cdot e^{i\mathbf{k}\cdot\mathbf{r}-i\omega t}\right) \Rightarrow$$

$$\Rightarrow i\mathbf{k}\times\mathbf{E} = i\omega\mu\mathbf{H}$$

$$\nabla \times \left(\mathbf{H_0} \cdot e^{i\mathbf{k}\cdot\mathbf{r}-i\omega t}\right) = \frac{\partial}{\partial t}\left(\varepsilon \cdot \mathbf{E_0} \cdot e^{i\mathbf{k}\cdot\mathbf{r}-i\omega t}\right) \Rightarrow \tag{1.6}$$

$$\Rightarrow i\mathbf{k}\times\mathbf{H} = -i\omega\varepsilon\mathbf{E}$$

So the following system of equations is obtained:

$$\begin{cases} \mathbf{k} \times \mathbf{E} = \mu\omega\mathbf{H} \\ \mathbf{k} \times \mathbf{H} = -\varepsilon\omega\mathbf{E} \end{cases} \tag{1.7}$$

From these equations it follows that the vectors k, E and H form a right-handed vector triad when a plane wave propagates in an electrical medium with μ and ε positive. On the contrary, if μ and ε are both negative the triad is left-handed and the Poynting vector, defined as S = E × H, is antiparallel to the wave vector k. Moreover, for the preservation of causality, the index of refraction of these materials, defined as n = ± root| εr | | μr |, assumes a negative sign. Due to these last two properties, materials with ε and μ simultaneously negative, take the name of left-handed materials or materials with index of negative refraction.

As described by Veselago in his work, these materials would have properties that are completely out of the ordinary. Consider, for example, the refraction of light in positive refractive index materials. When an electromagnetic wave propagates from a medium with refractive index n_1 to one with refractive index n_2, its direction of propagation θ_1 with respect to the normal, is deviated along the direction θ_2 defined by Snell's law:

$$n_1 \text{sen}\theta_1 = n_2 \text{sen}\theta_2 \tag{1.8}$$

What happens if, on the other hand, the light propagates by passing from a medium with a positive refractive index to one with a negative refractive index? In this case, the angle of entry and the exit one must have sine of opposite sign to continue to satisfy the law of Snell:

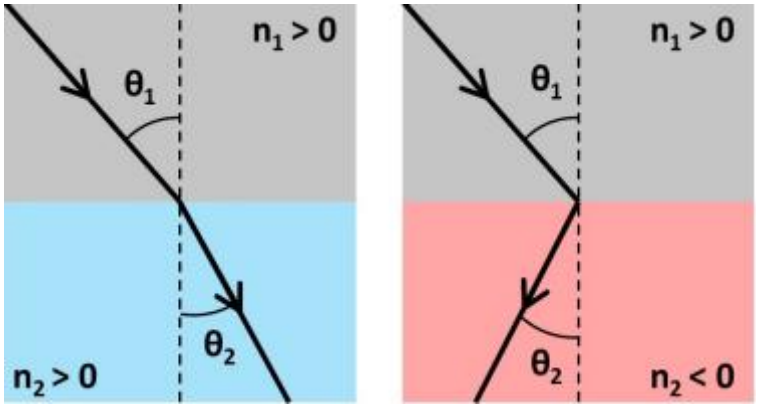

Fig.2 Snell'law for a negative refraction index medium

After Veselago theoretical description of the properties of these materials in 1968, the first experimental realization took place in 1996, when the English physicist John Pendry made a system capable of bypassing the limits imposed by nature, thus creating the first metamaterial.

The idea is, theoretically, very simple. It is, in fact, possible to recreate materials in the laboratory with optical properties that can be engineered at will, starting from common materials but organizing them into single elements (known as meta-atoms) distributed periodically or in a randomic system, and having dimensions and spacings smaller than the wavelength of the electromagnetic radiation with which they interact. In this way, in fact, the microscopic properties of each meta-atom appear to be "invisible" to electromagnetic radiation and the response of the material is affected by the behavior of the totality of all meta-atoms together. In other words, the inhomogeneous set of meta-atoms can be described, from the macroscopic point of view, as an homogeneous medium characterized by effective electrical permittivity and magnetic permeability ε_{reff} and μ_{reff}. On the base of these observations, Pendry firstly demonstrated the properties of a periodic array of wires of copper which, with specific dimensions, exhibited an

electromagnetic response with negative electric permittivity, then proposed a set of split ring resonator distributed as arrays (antennas in the form of rings not completely closed) which exhibited negative magnetic permeability. The combination of the two structures finally led to the construction of a structure in which simultaneously had $\mu r < 0$ and $\varepsilon r < 0$ in the microwave spectral region: the first metamaterial. [1][2][3].

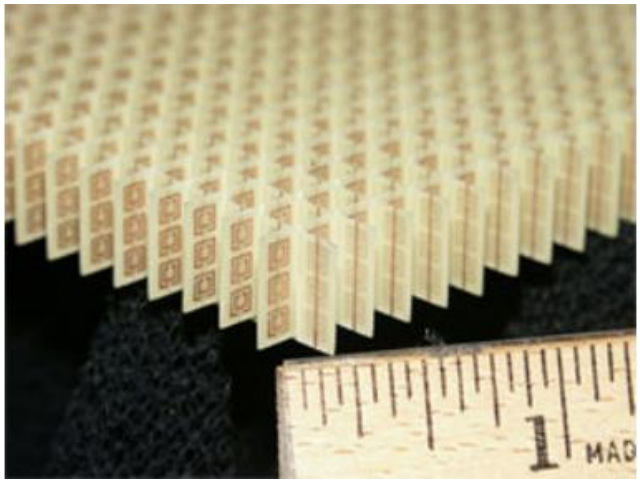

Fig.3: the combination of periodic array of wires of copper and a set of split ring resonators contributed to the creation of the first metamaterial

1.2 RIS: RECONFIGURABLE INTELLIGENT SURFACE

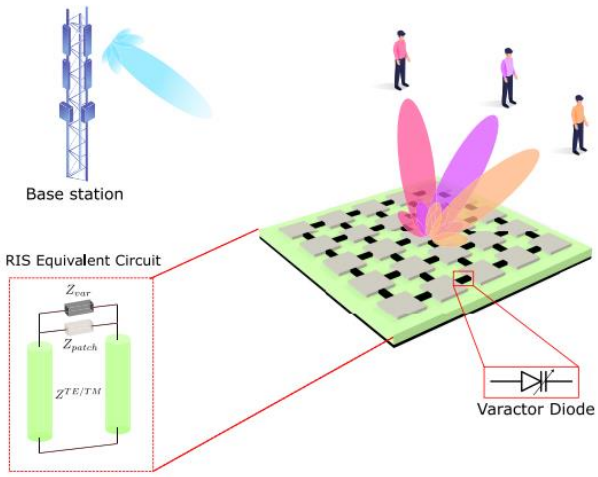

Fig. : 3D representation of metasurface in an open environment.

An evolutive step of metamaterial concept are the RIS, reconfigurable intelligent surfaces, engineered structures that are able to control the wavefront (phase, amplitude, frequency, and even polarization) of the impinging signals without the need of laborious decoding, encoding, and radio frequency processing operations.

The RISs are artificial electromagnetic (EM) surfaces with integrated electronics that are electrically controlled and have special wireless communication abilities.

The unique feature of RISs is that they enable telecommunications operators to manage the environment, and also to fully direct and totally shape the electromagnetic (EM) response of the distributed environmental objects.

The term "smart radio environments" has emerged as a result of RISs. A smart radio environment is a wireless network where the environment is transformed into a smart reconfigurable space that actively participates in information transfer and processing, in contrast to current wireless networks where the environment is out of the control of the telecommunication operators. The idea of software networks is further expanded in smart radio contexts. Future wireless networks in particular are quickly moving toward a platform that is software-based and reconfigurable, where every component of the network will be able to adjust itself to environmental changes.

A brand-new technology called RIS-enabled smart radio environments has the ability to drastically revolutionize how wireless networks are currently planned and optimized.

By manipulating how radio waves interact with nearby objects that are covered with thin, programmable layers of EM material, it is possible to counteract the adverse implications of natural EM propagation, which are highly probabilistic in nature.

By coherently combining the radio waves reflected, refracted, and scattered from vast surfaces, the RISs enable network planners to limit the damaging effects of multipath fading [1][2][3][21].

The following distinguishing characteristics relate to RISs:

• They are almost passive, and in an ideal situation, they would not require a separate energy source.

• They are seen as a continuous surface, where every point should theoretically be able to influence the wave impinging upon it (soft programming).

• Since they ideally do not require analog-to-digital/digital-to-analog converters (ADCs and DACs), and power amplifiers, they are not impacted by receiver noise.

They consequently offer an inherent full-duplex transmission and don't amplify or introduce noise while reflecting the signals.

• They can operate at any operational frequency, so they have full-band responsiveness.

• They are simple to apply, for example, to building facades, factory ceilings, internal spaces, human clothes, etc.

A sent radio signal typically hits a number of objects in a wireless communication environment, resulting in reflected, diffracted, and scattered copies of the original signal. These copies, which are referred to as multipath components, arrive at the receiver with various magnitudes, phases, and delays that, when added together in both constructive and destructive ways, significantly distort the received signal.

In wireless communications, this process is referred to as fading, and it is a significant barrier to the development of current and future wireless communication systems. By meticulously re-engineering the propagation of the EM waves in a software-controlled manner, RISs are used primarily to produce a controllable radio environment in which the extremely stochastic wireless channel is transformed into a deterministic space.

1.2.1 CONVENTIONAL TWO-RAY SYSTEM MODEL

In this model, the received signal consists of two components: the line-of-sight (LOS) ray and the ray reflected from the ground.

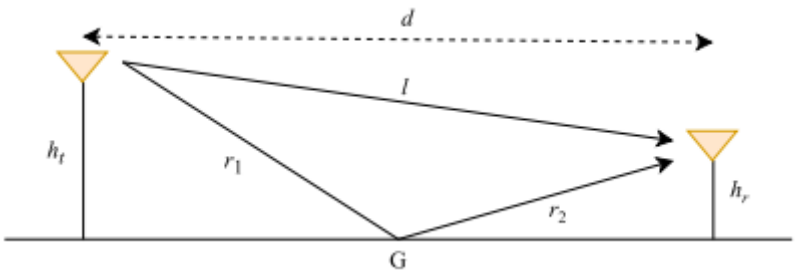

Fig.4 Two ray system model

We assume that the ground-plane only creates specular reflections and is reasonably large in relation to the transmission wavelength. The propagation of radio waves modeled as rays adhere to the Fermat's principle, which states that the path taken by a ray between two points is the path that is traversed in the least time.

The distance between the transmit and receive antennas is denoted by l, and the distance between the point of reflection G and the transmit and receive antennas are denoted by r1 and r2, respectively.

Considering x(t) the complex baseband transmitted signal and τ the relative time delay between the ray reflected from the ground and the LOS path, which is given by $\tau = (r1 + r2 - l)/c$ with c being the speed of light, we have: $x(t) \approx x(t - \tau)$

The (noise-free) baseband signal that was received can then be described as follows:

$$r(t) = \frac{\lambda}{4\pi}\left(\frac{e^{-\frac{j2\pi l}{\lambda}}}{l} + \frac{R \times e^{-\frac{j2\pi(r_1+r_2)}{\lambda}}}{r_1 + r_2}\right)x(t) \tag{2.1}$$

The LOS and ground-reflected signals, which have phase delays of :

$2\pi l/\lambda \quad 2\pi(r_1 + r_2)/\lambda,$

These are proportionate to propagation distances and are added to create the received signal. The received power Pr can be defined in terms of Pt as follows, assuming that the transmit power of x(t) is Pt:

$$P_r = P_t\left(\frac{\lambda}{4\pi}\right)^2\left|\frac{1}{l} + \frac{R \times e^{-j\Delta\phi}}{r_1 + r_2}\right|^2 \tag{2.2}$$

Where:

$\Delta\phi = \frac{2\pi(r_1+r_2-l)}{\lambda}$

is the phase difference between the two paths.

Assuming that the distance d is large enough, considering d much higher than ht + hr , then we obtain $d \approx l \approx r1 + r2$ and $R \approx -1$ for a specular reflection from the ground.

The previous equation can be reduced into:

$$P_r \propto P_t \left(\frac{1}{d^2}\right)^2 \tag{2.3}$$

This means that the received power decays with the fourth power of the distance *d*.

In the case in which the ground reflection is not present, the second term of the previous equation would not be present so the received power given just from the LOS propagation decays with the second power of the distance:

$$P_r = P_t \left(\frac{\lambda}{4\pi d}\right)^2. \tag{2.4}$$

Is it possible to clearly see the damaging effect that the unregulated reflection from the ground creates due to the two pathways' misaligned phases on the received signal's power. Even in the most optimistic transmission scenario with no user mobility and no random environmental impacts, a single unpredictable reflection from the ground may significantly reduce the received signal strength.

1.2.2 TWO-RAY SYSTEM MODEL WITH A SINGLE RECONFIGURABLE META-SURFACE

Let's have a look at the identical system model with the addition that a reconfigurable meta-surface has been placed on the ground to facilitate communication between the transmitter and receiver. To be more specific, we consider the simplest case study where the meta-surface functions as a reflecting surface and has the ability to change the direction of the reflected ray.

We take for granted that a reconfigurable meta-surface covers the entire ground. Conceptually, the reconfigurable meta-surface can be thought of as a perfect phase shifter that can change the reflected wave's phase to ensure that the LOS and reflected rays add up coherently and provide the strongest signal possible.

The following results would be obtained if we assumed that the reconfigurable meta-surface is capable of coherently synchronizing the phases of the direct and reflected rays

for any angles of incidence and reflection in order to optimize the phase of the reflected ray in an optimal manner:

$$P_r = P_t \left(\frac{\lambda}{4\pi}\right)^2 \left|\frac{1}{l} + \frac{1}{r_1 + r_2}\right|^2 \approx 4P_t \left(\frac{\lambda}{4\pi d}\right)^2 \tag{2.5}$$

We demonstrate that the usage of reconfigurable meta-surfaces has the ability to alter the scaling rule that determines how much power is received as a function of distance: the received power now only decays with the second power of distance, which is the same as the LOS ray, rather than the fourth [1][2][3][4][5][22].

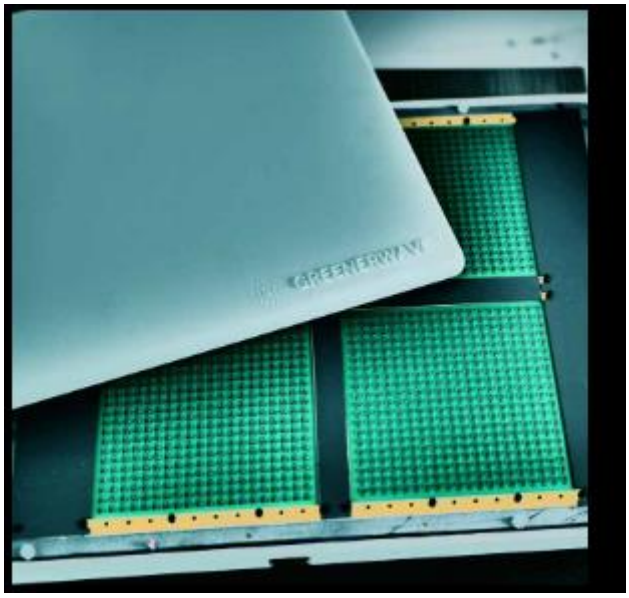

Fig 5. : Greenerway metasurface present in UNIVPM university, composed of four blocks of 400 varactor diodes

1.3 FDTD

The Finite-Difference Time-Domain (FDTD) is a numerical analysis technique used for modelling the interaction of electromagnetic fields with physical objects and devices in a specific environment, this technique is also known as computational electrodynamics.

Due to the irregular geometries that real devices typically have, this technique can be utilized to solve a variety of electromagnetic problems that cannot be analytically calculated. It offers a benefit as a simulation and analysis tool for challenging electromagnetic research and uses computer programs to identify approximations of the solutions to the underlying differential equation system. [6]

1.3.1 HISTORY OF FDTD

Maxwell's equations were formulated in 1873, and until 1960 there were not exact analytical solutions to these equations in cases of complex and asymmetrical geometries. The development of computer technologies from 1960 stimulated researchers to investigate the use of numerical methods to overcome the limitations of classical ones, in particular, for the accurate characterization of complex geometry.

Finite element method (FEM) is a widely used numerical method for solving partial differential equations in two or three space variables, that subdivides a large system into smaller, simpler parts that are called finite elements. This subdivision of the whole domain into simpler parts allows an accurate description of complex geometry and inhomogeneous materials and an easy representation of the total solution.

Method of Moments (MoM) is a rigorous, full-wave numerical technique for solving open boundary electromagnetic problems. The MoM is an integral equation technique, and it solves the integral form of Maxwell's equations instead of their differential forms which are used in the finite element methods.

The Finite Difference Time Domain (FDTD) method is an application of the finite difference method to solve Maxwell's equations. In FDTD, space is divided into small portions called cells. On the surfaces of each cell, there are assigned points and each point in the cell is required to satisfy Maxwell's equations. In this way, electromagnetic waves are simulated to propagate into a numerical space, almost as they do in real physical world.

The FDTD method had been presented for the first time by Kana Yee in 1966 [6], while the name and acronym "FDTD" were thought by Allen Taflove in 1980 [7]. This method is considered the simplest (in terms of implementation but also as a concept) of the full-wave numerical techniques and employs finite differences as approximations to both the spatial and temporal derivatives that appear in Maxwell's equations to solve

electromagnetic field problems in many applications and fields of work, ranging from the design of antennas to bio-photonics. It can solve complicated problems and analyze electromagnetic phenomena at radio and microwave frequencies, the only issue is that it is used to be computationally expensive, in fact, solutions may require a large amount of memory and computation time [7]. The advantages of FDTD can be summarized as its ability to work with a wide range of frequencies, devices, and environments, considering the advantage of computational efficiency for large problems compared to other techniques [8].

1.3.2 YEE'S ALGORITHM

In his renowned research article "Numerical solution of initial boundary value problems using Maxwell's equations in isotropic media," in 1966 Yee established a method for solving both electric and magnetic fields in time and space using coupled Maxwell's curl equations [7].

Yee's algorithm uses a set of finite-difference equations and a discretization of the structure geometry (grid of the space described as x, y, and z) to evaluate the two fields simultaneously, starting with the time-dependent Maxwell's curl equations in an isotropic medium.

The result is a system of linear equations (referred to as "update equations") in which the values of the electric field vector components in a volume of space are solved at one instant in time and the magnetic field vector components in the same spatial volume are solved at the next instant in time. The procedure is repeated until the required transient or steady-state electromagnetic field behavior has been achieved.

As a result, the FDTD algorithm gives a mechanism for obtaining future fields from past fields, and this method is known as a leap-frog method, in which one field is advanced before the other, and then the process is repeated.

Transition from Maxwell's equations to a set of finite difference equations

Maxwell's equations in a linear, isotropic nondispersive medium are given by:

$$\nabla \times \vec{E} = -\frac{\partial \vec{B}}{\partial t}$$
$$\nabla \times \vec{H} = \sigma \vec{E} + \frac{\partial \vec{D}}{\partial t} \tag{3.1}$$

$$\begin{cases} \vec{B} = \mu \vec{H} \\ \vec{D} = \varepsilon \vec{E} \end{cases} \tag{3.2}$$

Here $\vec{E}$ is the electric field vector in volts per meter, $\vec{D}$ is the electric flux density vector in coulombs per square meter, $\vec{H}$ is the magnetic field vector in amperes per meter, $\vec{B}$ is the magnetic flux density vector in webers per square meter, μ is the magnetic permeability in henrys per meter and ε is the electric permittivity in farads per meter. Moreover, in order to account the electric loss mechanisms that can dissipate electromagnetic fields in materials, an equivalent electric current $\sigma\vec{E}$ is defined where σ is the electric conductivity in siemens per meter [8].

Assuming that: μ, σ and ε are all time-independent, it's possible to decompose the electric and magnetic fields into an equivalent system of scalar equations which are the vector components of the fields represented in the three-dimensional rectangular coordinate system (x, y, and z):

$$\begin{cases} \frac{\partial E_y}{\partial z} - \frac{\partial E_z}{\partial y} = \frac{\partial B_x}{\partial t} \\ \frac{\partial E_z}{\partial x} - \frac{\partial E_x}{\partial z} = \frac{\partial B_y}{\partial t} \\ \frac{\partial E_x}{\partial y} - \frac{\partial E_y}{\partial x} = \frac{\partial B_z}{\partial t} \end{cases} \tag{3.3}$$

$$\begin{cases} \frac{\partial H_y}{\partial z} - \frac{\partial H_z}{\partial y} = \sigma E_x + \frac{\partial D_x}{\partial t} \\ \frac{\partial H_z}{\partial x} - \frac{\partial H_x}{\partial z} = \sigma E_y + \frac{\partial D_y}{\partial t} \\ \frac{\partial H_x}{\partial y} - \frac{\partial H_y}{\partial x} = \sigma E_z + \frac{\partial D_z}{\partial t} \end{cases} \tag{3.4}$$

It will be able to determine the six finite difference equations that form the basis of the Finite-Difference Time-Domain approach by starting with a system of six coupled partial differential equations and using one space-time discretization.

1.3.3 SPATIAL AND TEMPORAL DISCRETIZATION

There are limits on how large a temporal step may be in FDTD simulations; if it is too large, the technique gives unstable results. Furthermore, even when the precise region of interest is tiny, a spatial and temporal discretization is required in most cases to simulate magnetic problems that exist in an unbounded environment [8].

To utilize the FDTD algorithm, the first step is to define the problem region, divide the structure shape into cells of space with dimensions Δx, Δy and Δz, and select the time step at which the electromagnetic field must be evaluated.

The Yee algorithm divides space into a three-dimensional grid, known as the Yee cube or Yee space lattice, in which the E and H components are centred. Every circulating E component is surrounded by four circulating H components, and every circulating H component is surrounded by four circulating E components. With a space resolution specified by the size of the lattice unit cell, it is possible to obtain an approximation of the surface and internal geometry of the structure of interest using the Yee cube.

In a leap-frog structure, the method also centers the E and H components in time. Using H data already stored in the computer memory, all of the E computations in the three-dimensional space are completed and stored for a specific time point. The H computations are then finished and stored using the E data that was just computed. The cycle can start all over again, and the procedure will continue until the time-step is finished.

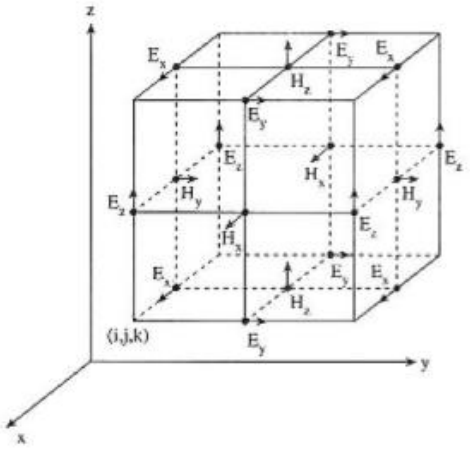

Fig.6: Position of the electric and magnetic field vector components about a cubic unit cell of the Yee space lattice. The electric field components are placed along the cube edges, while the magnetic field components are on the cube face

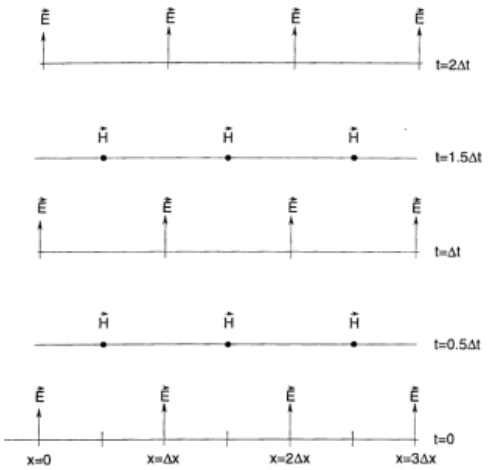

Fig.7: *Space-time chart of the Yee algorithm for a one-dimensional wave propagation. Initial condition for both electric and magnetic fields are zero everywhere in the grid*

1.3.4 SYSTEM OF FINITE DIFFERENCE EQUATIONS

After analyzing the problem, the length of the edge of the cubes that make up the grid and the duration of a temporal step can be determined. Assume that a grid point in the space is denoted as:

$$(i, j, k) = (i\Delta x, j\Delta y, k\Delta z) \tag{3.5}$$

and that each space-time function is evaluated at a discrete grid point and a discrete time point as follows:

$$F(i\Delta x, j\Delta y, k\Delta z, n\Delta t) = F_n(i, j, k) \tag{3.6}$$

where $n\Delta t$ denotes the point in time where F is being considered.

The partial space derivative of F can be replaced with the incremental ratios below using the introduced notation:

$$\begin{cases} \frac{\partial F}{\partial x} = \frac{F|^n_{i+1,j,k} - F|^n_{i,k,j}}{\Delta x} + O((\Delta x)^2) \\ \frac{\partial F}{\partial y} = \frac{F|^n_{i,j+1,k} - F|^n_{i,k,j}}{\Delta y} + O((\Delta y)^2) \\ \frac{\partial F}{\partial z} = \frac{F|^n_{i,j,k+1} - F|^n_{i,k,j}}{\Delta z} + O((\Delta z)^2) \\ \frac{\partial F}{\partial t} = \frac{F|^{n+1}_{i,j,k} - F|^n_{i,k,j}}{\Delta t} + O((\Delta t)^2) \end{cases} \tag{3.7}$$

A numerical approximation of the Maxwell's curl equations in three dimensions, given by previous equations, is produced using relatively easy mathematical passages and observations.

Consider the system's first equation, which is repeated for convenience:

$$\frac{\partial E_y}{\partial z} - \frac{\partial E_z}{\partial y} = \mu \frac{\partial E_x}{\partial t} + \sigma^* H_x \tag{3.8}$$

passing through the partial derivatives calculated in a point of the grid (i,j, k), we obtain:

$$\frac{1}{\mu_{i,j,k}} \left(\frac{E_y|^n_{i,j,k+\frac{1}{2}} - E_y|^n_{i,j,k+\frac{1}{2}}}{\Delta z} - \frac{E_z|^n_{i,j+\frac{1}{2},k} - E_z|^n_{i,j+\frac{1}{2},k}}{\Delta y} - \sigma^*_{i,j,k} H_x|^n_{i,j,k} \right) = \frac{H_x|^{n+\frac{1}{2}}_{i,j,k} - H_x|^{n-\frac{1}{2}}_{i,j,k}}{\Delta t} \tag{3.9}$$

At time step n, all of the quantities on the left are assessed, including the magnetic field on the right, which is not expected to be stored in the computer's memory (only its preceding term), but is approximated using a semi-implicit approximation:

$$H_x\big|_{i,j,k}^{n+\frac{1}{2}} = \frac{H_x\big|_{i,j,k}^{n+\frac{1}{2}} - H_x\big|_{i,j,k}^{n-\frac{1}{2}}}{2} \tag{3.10}$$

substituting into the equation:

$$\begin{aligned} H_x\big|_{i,j,k}^{n+\frac{1}{2}} &= \left(\frac{1-\frac{\sigma^*_{i,j,k}\Delta t}{2\mu_{i,j,k}}}{1+\frac{\sigma^*_{i,j,k}\Delta t}{2\mu_{i,j,k}}}\right) H_x\big|_{i,j,k}^{n-\frac{1}{2}} + \left(\frac{\frac{\Delta t}{\mu_{i,j,k}}}{1+\frac{\sigma^*_{i,j,k}\Delta t}{2\mu_{i,j,k}}}\right) \cdot \\ &= \left(\frac{E_y\big|_{i,j,k+\frac{1}{2}}^{n} - E_y\big|_{i,j,k+\frac{1}{2}}^{n}}{\Delta z} - \frac{E_z\big|_{i,j+\frac{1}{2},k}^{n} - E_z\big|_{i,j+\frac{1}{2},k}^{n}}{\Delta y}\right) \end{aligned} \tag{3.11}$$

The finite-difference formulas for the other field components are defined using an analog technique:

$$\begin{aligned} H_y\big|_{i,j,k}^{n+\frac{1}{2}} &= \left(\frac{1-\frac{\sigma^*_{i,j,k}\Delta t}{2\mu_{i,j,k}}}{1+\frac{\sigma^*_{i,j,k}\Delta t}{2\mu_{i,j,k}}}\right) H_y\big|_{i,j,k}^{n-\frac{1}{2}} + \left(\frac{\frac{\Delta t}{\mu_{i,j,k}}}{1+\frac{\sigma^*_{i,j,k}\Delta t}{2\mu_{i,j,k}}}\right) \cdot \\ &= \left(\frac{E_z\big|_{i+\frac{1}{2},j,k}^{n} - E_z\big|_{i+\frac{1}{2},j,k}^{n}}{\Delta x} - \frac{E_x\big|_{i,j,k+\frac{1}{2}}^{n} - E_x\big|_{i,j,k+\frac{1}{2}}^{n}}{\Delta z}\right) \end{aligned}$$

$$\begin{aligned} H_z\big|_{i,j,k}^{n+\frac{1}{2}} &= \left(\frac{1-\frac{\sigma^*_{i,j,k}\Delta t}{2\mu_{i,j,k}}}{1+\frac{\sigma^*_{i,j,k}\Delta t}{2\mu_{i,j,k}}}\right) H_z\big|_{i,j,k}^{n-\frac{1}{2}} + \left(\frac{\frac{\Delta t}{\mu_{i,j,k}}}{1+\frac{\sigma^*_{i,j,k}\Delta t}{2\mu_{i,j,k}}}\right) \cdot \\ &= \left(\frac{E_x\big|_{i,j+\frac{1}{2},k}^{n} - E_x\big|_{i,j+\frac{1}{2},k}^{n}}{\Delta y} - \frac{E_y\big|_{i+\frac{1}{2},j,k}^{n} - E_y\big|_{i+\frac{1}{2},j,k}^{n}}{\Delta x}\right) \end{aligned}$$

$$\begin{aligned} E_x\big|_{i,j,k}^{n+\frac{1}{2}} &= \left(\frac{1-\frac{\sigma^*_{i,j,k}\Delta t}{2\varepsilon_{i,j,k}}}{1+\frac{\sigma^*_{i,j,k}\Delta t}{2\varepsilon_{i,j,k}}}\right) E_x\big|_{i,j,k}^{n-\frac{1}{2}} + \left(\frac{\frac{\Delta t}{\varepsilon_{i,j,k}}}{1+\frac{\sigma^*_{i,j,k}\Delta t}{2\varepsilon_{i,j,k}}}\right) \cdot \\ &= \left(\frac{H_z\big|_{i,j+\frac{1}{2},k}^{n+\frac{1}{2}} - H_z\big|_{i,j+\frac{1}{2},k}^{n+\frac{1}{2}}}{\Delta y} - \frac{H_y\big|_{i,j,k+\frac{1}{2}}^{n+\frac{1}{2}} - H_y\big|_{i,j,k+\frac{1}{2}}^{n+\frac{1}{2}}}{\Delta z}\right) \end{aligned} \tag{3.12}$$

$$E_y|_{i,j,k}^{n+\frac{1}{2}} = \left(\frac{1-\frac{\sigma_{i,j,k}^{*}\Delta t}{2\varepsilon_{i,j,k}}}{1+\frac{\sigma_{i,j,k}^{*}\Delta t}{2\varepsilon_{i,j,k}}}\right) E_y|_{i,j,k}^{n-\frac{1}{2}} + \left(\frac{\frac{\Delta t}{\varepsilon_{i,j,k}}}{1+\frac{\sigma_{i,j,k}^{*}\Delta t}{2\varepsilon_{i,j,k}}}\right) \cdot \left(\frac{H_x|_{i,j,k+\frac{1}{2}}^{n+\frac{1}{2}} - H_x|_{i,j,k+\frac{1}{2}}^{n+\frac{1}{2}}}{\Delta z} - \frac{H_z|_{i+\frac{1}{2},j,k}^{n+\frac{1}{2}} - H_z|_{i+\frac{1}{2},j,k}^{n+\frac{1}{2}}}{\Delta x}\right)$$

$$E_z|_{i,j,k}^{n+\frac{1}{2}} = \left(\frac{1-\frac{\sigma_{i,j,k}^{*}\Delta t}{2\varepsilon_{i,j,k}}}{1+\frac{\sigma_{i,j,k}^{*}\Delta t}{2\varepsilon_{i,j,k}}}\right) E_z|_{i,j,k}^{n-\frac{1}{2}} + \left(\frac{\frac{\Delta t}{\varepsilon_{i,j,k}}}{1+\frac{\sigma_{i,j,k}^{*}\Delta t}{2\varepsilon_{i,j,k}}}\right) \cdot \left(\frac{H_y|_{i+\frac{1}{2},j,k}^{n+\frac{1}{2}} - H_y|_{i+\frac{1}{2},j,k}^{n+\frac{1}{2}}}{\Delta x} - \frac{H_x|_{i,j+\frac{1}{2},k}^{n+\frac{1}{2}} - H_x|_{i,j+\frac{1}{2},k}^{n+\frac{1}{2}}}{\Delta y}\right)$$

It is possible to discover the electric and magnetic field components in any point of the grid and analyze the evolution of the electromagnetic field at each point of the chosen volume using the system of equations obtained from Yee notation.

1.3.5 NUMERICAL DISPERSION AND STABILITY

Numerical dispersion and stability are the two key criteria that influence the choice of time step, t, and lattice space increments, Δx, Δy and Δz, in the FDTD algorithm. Numerical dispersion is reduced to zero in a uniform one-dimensional grid, and the solution of a continuous one-dimensional wave equation, as given by the Yee algorithm, is precise. Instead, the numerical dispersion is affected by the direction of wave propagation in a two- or three-dimensional Yee space lattice, which means that the numerical wave's phase velocity differs from the vacuum speed of light. The modal wavelength, the direction of wave propagation in the grid, and the grid discretization all influence this variation. [9]

The physical phase-velocity error and the velocity-anisotropy error can be used to quantify numerical dispersion, with the physical phase-velocity error measuring the amount of phase lead or lag and the velocity anisotropy error measuring the wavefront distortion due to the anisotropy of the space lattice.

Physical phase-velocity error can be decreased by using the right grid discretization, as long as the problem geometry is kept as basic as feasible. As a result, discretization must meet two criteria: computational stability and precision.

Proper cell size selection yields meaningful findings, which is satisfied if the grid's linear dimension is a fraction of the wavelength present in the problem under investigation.

Using a cubic grid with Δx = Δy = Δz as the starting point, the accuracy improves under the condition:

$$\Delta x < \frac{\lambda_{min}}{10} \tag{3.13}$$

The Courant–Friedrichs–Lewy criterion, on the other hand, must be satisfied in time for computational stability. Thus, in the case of cubic cells, the linked numerical system's stability is maintained if the chronological step is as follows:

$$\Delta t \leq \frac{1}{c_0\sqrt{\frac{1}{(\Delta x)^2}+\frac{1}{(\Delta y)^2}+\frac{1}{(\Delta z)^2}}} = \frac{1}{c_0\frac{\sqrt{3}}{(\Delta x)}} = \frac{\Delta x}{c_0\sqrt{3}} \tag{3.14}$$

$$S = \frac{c_0\Delta t}{\Delta_x} = \frac{1}{\sqrt{3}} \tag{3.15}$$

The Courant number, commonly referred to as the stability factor, is a dimensionless quantity.

The stability criterion is satisfied if the FDTD algorithm is quicker than the propagation wavelength, according to equations and. When the S value is exceeded, the results diverge after a few rounds, resulting in the program failing since the results can no longer be represented.

More than the stability of the Yee method determines the whole FDTD solution procedure for Maxwell's equations.

The study of stability up to this point had centered on the numerical stability of the basic Yee method in Cartesian coordinates. However, the whole FDTD procedure's stability is dependent on more than this factor. A challenge of generalized stability occurs as a result of interactions between the Yee algorithm and any augmenting algorithms used to model boundary conditions, variable meshing and complex materials [10].

1.3.6 BOUNDARY CONDITIONS

It is common practice to truncate the computational domain to a finite domain when computationally modeling wave propagation processes in a domain that extends to infinity.

To reduce undesirable numerical effects, the newly established external boundary is somewhat artificial.

There is a requirement for specific treatment at these boundaries due to reflections.

In FDTD, the solutions found from the Yee algorithm are extended to an infinite domain and

is possible to use suitable boundary conditions on the outer perimeter of the domain once the electric and magnetic fields on the external surface of the region of interest are known.

RBCs, or Radiation Boundary Conditions, and ABCs, or Absorbing Boundary Conditions, are two forms of boundary conditions that differ in their theoretical basis. Even though both produce faults, false reflections, the ABCs solutions are the most commonly utilized with the FDTD approach.

Gerrit Mur was the first to address the search for adequate boundary conditions in 1981.

Mur's solution is the first viable response to the boundary condition problem for methods that use a spatial grid to solve Maxwell's equations, and because of its simplicity and computational economy, it is a good choice for problems that do not require a high precision solution.

Although to obtain simulations, all of the ABCs results obtained from Mur and others who published their works before 1994 yield effective outer-boundary reflection coefficients around -35 and -45dB.

A 40 dB reduction in the effective reflection coefficient is required for optimum dynamic range [9].

Furthermore, they have a constraint in the case of an oblique incident wave because, in particular for the oblique waves cannot be absorbed in the first order Mur's solution, hence they are reflected inside the boundary.

Berenger introduced the perfectly matched layer (PML) for Maxwell's equations that represent the alternative that allows you to get around these restrictions.

It consists in dividing the components of the electric or magnetic field in the absorbing boundary region are broken down into a subcomponent that can be perfectly absorbed by the perfectly matched layer material.

As a result, a nonphysical absorbing medium close to the outer FDTD mesh border is created, with a wave impedance independent of the angle of incidence and frequency of outgoing scattered waves. As a result, when a wave exceeds the boundary of the region of interest, it is not reflected but attenuated exponentially. This method permits the maximum dynamic range to be increased to greater than 80 dB [10].

The PML ABC has a combination of broadband effectiveness, robustness, and computational efficiency that no other ABC has. However, it is important to remember that the absorbing boundary condition has no real equivalent; they are mathematical schemes applied at the 26 artificial numerical boundaries of a computational domain to minimize or eliminate spurious reflections that occur in wave propagation simulations. [11]

Variable and unstructured meshing:

The FDTD algorithm is based on a Cartesian lattice that is orthogonal and regular. The first-order derivatives of Maxwell's equations can be approximated using central-difference operators due to the grid's orthogonality and consistent spacing between grid points. This yields a discrete approximation for the fields based on a uniform orthogonal lattice and a second-order accurate solution in space and time.

Structures with fine geometrical features, on the other hand, are not always able to adhere to the edges of the uniform lattice.

A significant mistake in the computation can occur in situations where the field interaction is heavily reliant on the shape of the boundary and the grid does not adapt to the geometry of the boundary - such as a curved or planar boundary.

This is why the boundary constraints must be enforced on an auxiliary boundary, which is a staircase approximation of the physical boundary, rather than directly on the boundary.

To depict the local fields accurately, it is occasionally necessary to employ non-uniform grids and reduce the actual cell size.

Sheen presented a quasi-uniform grid FDTD technique in 1991.

The spatial derivatives of the fields at the interface between the two regions can be stated using central-difference approximations in this manner, resulting in a second order correct formulation.
The method is confined to specific geometries that comply to this specialized grid, but the nonuniform FDTD algorithm is a powerful and versatile tool for complicated and highly detailed circuits with rectangular geometries [12].

Lossy, dispersive, nonlinear, and gain materials:
Understanding the nature of pulse interactions with materials over large bandwidths is required for controlling or processing brief electromagnetic pulses.
Material dispersion, nonlinearity, and gain are all important factors in shortpulse physics [9].
Linear Dispersion: At low intensities of electromagnetic waves, the permittivity and/or permeability of a material fluctuates with frequency.
Nonlinearity: The dielectric permittivity and/or permeability of a material fluctuates with the local strength of an electromagnetic wave interaction, especially at high intensities
Nonlinear dispersion: The interaction electromagnetic wave's sinusoidal frequency content affects the strength of a material's nonlinear properties.
Gain: provides an exponential rise in the interaction wave with propagation distance in the material, rather than an exponential loss as in traditional materials. Gain is usually a function of the interacting wave's frequency and strength, but it can also be frequencydispersive and nonlinear [9][12].

1.4 S.A.R.

The body can be viewed as a lossy, dielectric entity with free space's magnetic permeability from an RF electromagnetic perspective. Electromagnetic fields enter the human body at microwave and radio frequencies, where they engage with biological tissue in a variety of ways.
The most significant of which are explained by the passage of energy from the biological substance to an electromagnetic field. A term typically used to describe electromagnetic

radiation is the specific absorption rate which is determined by field interaction with biological tissue (SAR).

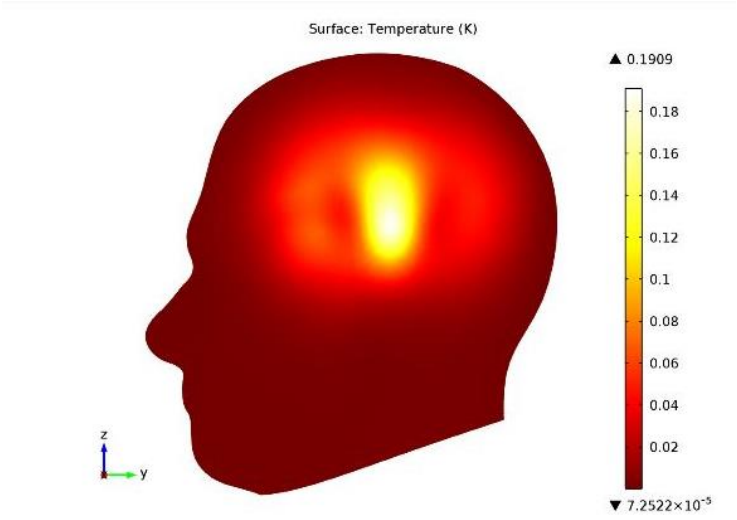

Fig.8 :Local increase in temperature just under the cell phone

The SAR value, which is measured as the rate at which energy is absorbed per unit mass by a human body or by a small sample volume when exposed to a radio frequency (RF) electromagnetic field, is defined by the International Electrotechnical Commission (IEC) standard as units of power per mass of tissue (W/kg) [13].

The current created in the body irradiates the nerves when the human body is exposed to low-frequency electromagnetic radiation (1Hz to 100KHz). Instead, exposure to high-frequency electromagnetic waves (100Hz–10GHz), as those emitted by mobile phones, triggers a heating reaction that can raise body temperature. SAR is the word now in use in both national and international dosimetry to describe the thermogenic features of the electromagnetic field and to provide an indirect quantitative measure of RF energy to ensure that they meet the safety recommendation guidelines set by FCC and CENELEC. Formally speaking, the SAR is the time derivative of the incremental energy absorbed by (dissipated in) an incremental mass contained in a volume of a specific density. In contrast, at a specific location in the tissue material, it is related to electric fields by [14]:

$$SAR = \frac{\sigma |E|^2}{\rho} \tag{4.1}$$

where σ and ρ are, respectively, the sample electrical conductivity (S/m) and sample density (kg/m3), and E (the effective value of the electric field created in the body). This definition makes it clear that the SAR, which is directly related to the fields inside the body, is a suitable indirect non-thermal measure for the interaction of electromagnetic fields with human tissue.

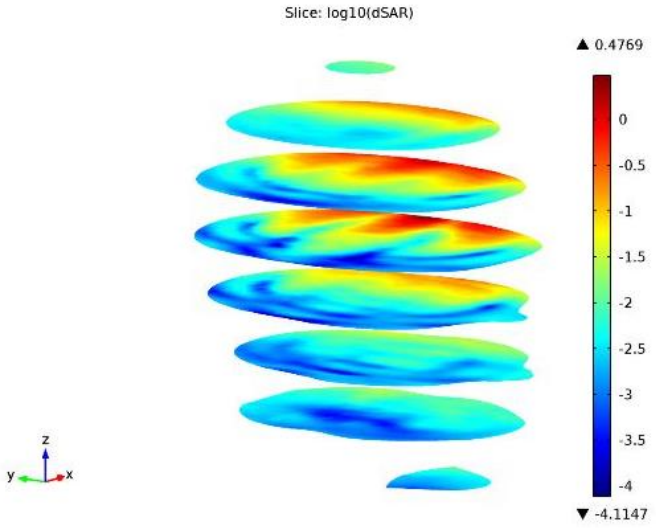

Fig. 9: Plot showing local SAR value in the brain tissue.

This assertion appears to be true if we assume that all biological actions, whether thermal or not, are directly related to the internal electric field. Additionally, SAR measures the power absorbed by a geographical region (sample volume) exposed to the source's emission rather than measuring the emission from the source of electromagnetic energy. The average SAR, which is determined from the previous equation by integrating across the full exposed volume V of the body or body portion under discussion, is a more useful quantity for biological interaction considerations [13]:

$$SAR = \frac{1}{V}\int_{sample} \frac{\sigma(r)\left|\vec{E}(\vec{r})\right|^2}{\rho(r)} \mathrm{d}r \tag{4.2}$$

Since the tissue of the human body are very different from each other for geometric characteristic as well as for density, SAR values will not be uniform over the entire region in which the power emitted by the electromagnetic field will be absorbed but will change significantly between one tissue and another [15].

The SAR value depends solely on the geometrical characteristics of the body component involved in the emission of the electromagnetic waves because it is directly proportional to the electrical conductivity of the substance under investigation. In actuality, the electrical conductivity is dependent on the specimen's shape and is defined as the electrical resistance of the material multiplied by the cross-sectional area to length ratio. Additionally, SAR is inversely proportional to the density of the substance that the electric field radiates and directly related to the Root Mean Square of the intensity of the electric field [16]. Other factors can affect the SAR value, including:

- The incident field parameters, which include the irradiated subject's intensity, frequency, polarization, and configuration, as well as the near- and far-field circumstances.
- The antenna's placement on the body affects the SAR distribution.
- The thickness-dependent dielectric characteristics of the different tissues and the reflection of other items in the radiation field.

1.4.1 DOSIMETRY

The frequency, strength of the electric (E) and magnetic (H) fields, as well as their direction and orientation, are characteristics of radio waves in free space. For any meaningful and widespread quantification of biological data gathered experimentally, it is vital to identify these fields because only the electromagnetic fields inside the tissues may interact with biological systems.

Dosimetry, which is used to measure how much energy is taken up by the body as a result of exposure to radiofrequency electromagnetic fields, makes an effort to gauge these interactions.

The term "bioelectromagnetic" is derived from the dosimetric notion, where the dose is the energy per unit mass. Theoretical and experimental research have been growing in parallel but complementary ways in the field of bioelectromagnetics [13].

1.4.2 THEORETICAL DOSIMETRY

Theoretical dosimetry is the study of whole body and localized SAR distributions predicted by sophisticated mathematical models that closely resemble real humans or animals. When employing several numerical anatomical models, theoretical dosimetry identifies how anticipated SAR varies in proportion to permittivity values for various tissue types (muscle, fat, skin, bone, and marrow). Localized SAR values are highly dependent on permittivity values, although whole body SAR is not very sensitive to variations in them.

There is no standardized method for calculating the relative influence on SAR values due to the complicated interplay between permittivity and projected SAR values in various anatomical models.

The main instrument for assessing EMF exposure is the development of theoretical dosimetry modeling methodologies and powerful computer hardware, while numerical dosimetry is defined as the determination of energy absorption values in tissue material using numerical simulation approach.

1.4.3 EXPERIMENTAL DOSIMETRY

The development of techniques and tools suited for measuring internal electric fields, whole-body or localized SAR values, or associated variables, is the focus of experimental dosimetry.

Carefully planned experiments are essential for validating theoretical hypotheses and identifying their limitations. When employing heterogeneous digital anatomical models and anticipated localized SAR values that deviate significantly from whole body average SAR ("hot or cold" areas), the discrepancy between empirical and theoretical techniques is higher.

The fact that SAR alone does not adequately describe the regional thermal environment and does not take into consideration the thermoregulatory factors (convection by blood flow and conduction) is further evidenced by this incongruity [18].

1.4.4 OVERVIEW OF DIELECTRIC PROPERTIES

Polarization, a phenomena that happens when internal charge in a material moves in reaction to an external electric field, is the most significant impact that results from the interaction of an electric field with a dielectric substance. Each type of induced dipole exhibits a distinct polarization in a given molecule, whether it be permanent, transitory, or induced. Ionic drift and multiple polarization mechanisms, each controlled by a different time constant, are the two effects of an electric field.

Conduction and displacement currents are established as a result. Biological materials are therefore categorized as lossy dielectric materials[19].

The total polarization at any given time is the vector sum of all contributions, including:

$$P = \sum_{i}^{n} P_i \tag{4.3}$$

The polarization P is related to the dielectric displacement D, the internal electric field strength E and the dielectric properties as follows:

$$D = \varepsilon_0 E + P \tag{4.4}$$

where ε is the permittivity of the medium and $\varepsilon 0$ is the permittivity of the free space. From this expression, the dependence of P on E can be defined as:

$$P = \varepsilon_0(\varepsilon - 1)E \tag{4.5}$$

which describe the polarisation P as a material-specific displacement vector and the medium permittivity as:

$$\varepsilon = \frac{P}{\varepsilon_0 E} + 1 \tag{4.6}$$

Since the relative permittivity can be a tensor, a complex parameter or simply a real number depending on the directionality of the response and the phase difference between the displacement vector and the electric field. Assuming a linear isotropic behaviour, the relative permittivity of biological materials $\varepsilon *$ is a complex parameter expressed as follows:

$$\varepsilon^* = \varepsilon' - j\varepsilon'' \tag{4.7}$$

where ε' is the real part and determines the component of the displacement current which is out-of phase with the driving field, while the imaginary part ε''relates to the in-phase or power loss component and is referred to as loss factor [17]. Considering displacement and ionic currents, a biological material is characterized by an effective loss factor defined as:

$$\varepsilon'' = \frac{\sigma}{\omega\varepsilon_0} \tag{4.8}$$

where σ is the total conductivity of the material which, depending on the nature of the sample and ω the angular frequency of the field. The SI unit of conductivity is siemens per metre (S·m−1) which presumes that in the above expression $\varepsilon 0$ is expressed in farads per metre (F·m−1) and ω in radians per second. So, the electrical properties of tissues can be present in terms of complex dielectric permittivity defined as effective complex relative dielectric permittivity:

$$\varepsilon^*_{r_{eff}}(\omega) = \varepsilon'_r(\omega) - j\left(\varepsilon''_r(\omega) + \frac{\sigma_{dc}}{\omega\varepsilon_0}\right) = \varepsilon'_r(\omega) - j\left(\frac{\sigma_{ac}(\omega) + \sigma_{dc}}{\omega\varepsilon_0}\right)$$

(4.8)

and the electrical conductivity of the medium is identified by the following quantity:

$$\sigma(\omega) = \sigma_{ac}(\omega) + \sigma_{dc} = \omega\varepsilon_0\varepsilon_r''(\omega) + \sigma_{dc}$$

(4.9)

where σdc (continuous) which represents the ohmic conductivity deriving from the mobility of the ionic species present in a specific tissue and σac (alternating) which represent losses due to dielectric relaxation [19][20]. The dielectric properties of a biological tissue result from the interaction of electromagnetic radiation with its constituents at the cellular and molecular level.

The main features of the dielectric spectrum of a biological tissue are:

• The relative permittivity of a tissue may reach values of up to 106 or 107 at frequencies below 100 Hz.

• It decreases at high frequencies in three main interaction mechanism known as the α, β and γ dispersions.

• Tissues have finite ionic conductivities commensurate with the nature and extent of their ionic content and ionic mobility

The polarization of water molecules results in permanent dipoles that are randomly oriented in the absence of an external field and field-oriented when an external field is applied, which causes the dispersion in the microwave frequency range (frequencies larger than 1 GHz).

The polarization of cellular membranes, which serve as barriers to the flow of ions between the intracellular and extracellular media, is the principal cause of the dispersion in the radio frequency band (from 20 kHz to about 300 GHz). The polarization of organic macromolecules like proteins and other organic compounds also contributes to the dispersion.

Ionic diffusion activities at the location of the cellular membrane are linked to the low frequency dispersion (below 10 kHz).

In its simplest form, each dispersion is characterized by a single time constant τ (dielectric relaxation constant) and exhibits the following frequency dependence:

$$\varepsilon_r^* = \varepsilon_\infty + \frac{\varepsilon_s - \varepsilon_\infty}{1 + j\omega\tau} \tag{4.10}$$

	ε_r		Conductivity [S/m]	
Frequency	**2 GHz**	**2.4 GHz**	**2 GHz**	**2.4 GHz**
Blood	60.50	60.12	18.01	17.01
Bone	20.86	20.63	4.75	4.83
Heart	57.08	56.43	15.75	15.07
Kidney	55.03	54.27	17.45	16.47
Liver	44.91	44.42	11.46	11.16
Muscle	54.44	54.16	11.69	11,29
Dry skin	38,53	38,03	11,41	10.82
Small intestine	56.66	56.03	24.04	21.94

Fig.10 : Dielectric constant and conductivity for different parts of the body at different frequencies

1.5 AIM OF THE STUDY

The development of a smart wirless environment, through which the electromagnetic fields can be redirect and managed could be also useful regarding the safety of biological tissues that are used to live and move inside this environment.

The main biological effect of the penetration of electromagnetic waves into the human body is heating. However, the levels we are normally exposed to are too low to cause significant warming. There are currently no known health effects caused by long-term exposure.

However, a smart use of reconfigurable intelligent surfaces could manage the electromagnetic fields in a way that they can be redirect more precisely on the everyday devices, so to avoid excessive exposure of biological tissues to radiofrequency e.m. fields.

The purpose of this study is divided into two parts:

- To develop an FDTD model of manually Reconfigurable Intelligent Surface, evaluating its working principles, its response to an incident plane wave by evaluating the electric field distribution over it.
- The building of an FDTD environment in which is simulated the presence of Metasurface, radiofrequency source, biologic tissue and a device. The aim is to do a series of simulations to prove that the presence of a metasurface would lead to less exposure of biologic tissues to radiofrequency, and there would be a significant redirection toward the electric device.

2. MATERIALS AND METHODS

2.1 ALLEN TAFLOVE'S DIODE MODEL IN A LUMPED CIRCUIT

All the simulation analysis have been carried out through FDTD technique, implemented with C programming language.

The first idea was to use a diode as first concept of meta-atom for the metasurface composition.

The use of a diode on a transmission line FDTD modelled by Taflove was the first step that have been done was to evaluate the effectiveness of the diode, firstly on a trasmission line in just one dimension, following the Taflove's model of elements into a lumped circuit.

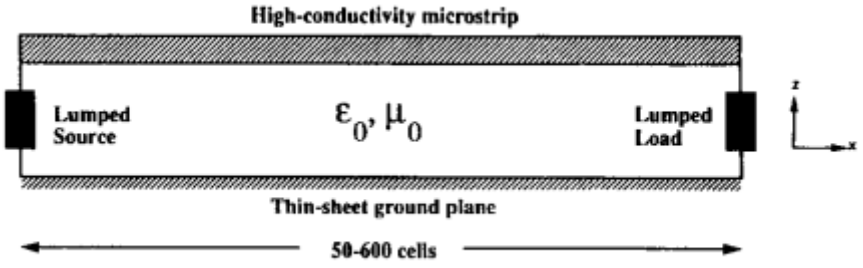

Fig.11 : Allen Taflove's generic geometry used for 3-D FD-TD models of a linear or nonlinear lumped element terminating a stripline.

The current through a lumped-circuit diode is expressed by:

$$I_d = I_0\left[e^{(qV_d/\mathbf{k}T)} - 1\right] \tag{5.1}$$

where **q** is the charge of an electron, **Vd** is the voltage across the diode, **k** is Boltzmann's constant, and **T** is the temperature in degrees Kelvin.

If one assumes a z-directed diode located in free-space at $Ez_{i,j,k}$, the electric field time-stepping relation is given by:

$$E_z\big|_{i,j,k}^{n+1} = E_z\big|_{i,j,k}^{n} + \frac{\Delta t}{\epsilon_o}\nabla \times H\big|_{i,j,k}^{n+1/2} - \frac{\Delta t}{\epsilon_o \Delta x \Delta y} I_0\left[e^{\left(-qE_z\big|_{i,j,k}^{n}\Delta z/\kappa T\right)} - 1\right]. \tag{5.2}$$

It has been determined that this expression yields a numerically unstable algorithm for diode voltages larger than 0.8 volts due to its explicit formulation which employs the previously computed electric field in the exponential. We have found that a numerically stable FD-TD algorithm for the lumped diode can be realized in 3-D by using the semi-implicit update strategy for the electric field.

$$E_z\big|_{i,j,k}^{n+1/2} = \frac{1}{2}\left(E_z\big|_{i,j.k}^{n+1} + E_z\big|_{i,j,k}^{n}\right). \tag{5.3}$$

To evaluate the real effectiveness of the diode, it has been built an FDTD 3-D dominium and a single strip with the diode placed at one extremity, then it was made of two metal strip, with the diode came from the taflove's model placed in between of the trasmission line.

The response from the trasmission line is done after the impinging of a 1 V/m incident plane wave with the following band : [1-8] GHz

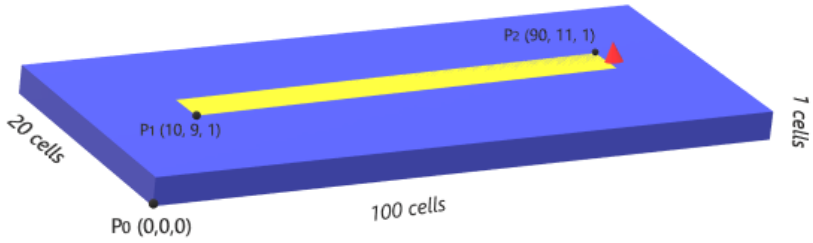

Fig.12: first concept of patch with the diode placed at the end of the trasmission line

We realized thath the plane wave didn't polarize the diode even if we provided it with really high values, in fact we arrived to provide until 1000000 V/m of wave to obtain really small values of diode polarization.

So we understood that the diode should have been substituted with another lumped element to constitute the meta-atom, it will be the varactor.

Consider Maxwell's curl H equation, suitable for time-stepping the E-field:

$$\nabla \times \boldsymbol{H} = \boldsymbol{J}_C + \frac{\partial \boldsymbol{D}}{\partial t} \tag{5.4}$$

$$\boldsymbol{J}_C = \sigma \boldsymbol{E}, \boldsymbol{D} = \varepsilon \boldsymbol{E}.$$

$$E_z\big|_{i,j,k}^{n+1} = \left(\frac{1 - \dfrac{\sigma_{i,j,k}\,\Delta t}{2\varepsilon_{i,j,k}}}{1 + \dfrac{\sigma_{i,j,k}\,\Delta t}{2\varepsilon_{i,j,k}}}\right) E_z\big|_{i,j,k}^{n} + \left(\frac{\dfrac{\Delta t}{\varepsilon_{i,j,k}}}{1 + \dfrac{\sigma_{i,j,k}\,\Delta t}{2\varepsilon_{i,j,k}}}\right) \left(\frac{H_y\big|_{i+1/2,j,k}^{n+1/2} - H_y\big|_{i-1/2,j,k}^{n+1/2}}{\Delta x} + \frac{H_x\big|_{i,j-1/2,k}^{n+1/2} - H_x\big|_{i,j+1/2,k}^{n+1/2}}{\Delta y}\right) \tag{5.5}$$

To the Maxwell's equations is added the parasite element, are added currents due to capacities or inductances, so we have to change the equation in that cell where there is the lumped element

$$\nabla \times \boldsymbol{H} = \boldsymbol{J}_C + \frac{\partial \boldsymbol{D}}{\partial t} + \boldsymbol{J}_L \tag{5.6}$$

To solve the next E field we need part of the previous one and the contribution of the average of the two

$$E_z\Big|_{i,j,k}^{n+1} = E_z\Big|_{i,j,k}^{n} + \frac{\Delta t}{\varepsilon_0}(\nabla \times \boldsymbol{H})_z\Big|_{i,j,k}^{n+1/2} - \frac{\Delta t}{\varepsilon_0 \Delta x \Delta y} I_L^{n+1/2} \tag{5.7}$$

To make the resistance R just change the values of the constants, modifying the coefficients in the equation (as if there were a cell with another dielectric constant)

$$E_z\Big|_{i,j,k}^{n+1} = \left(\frac{1 - \dfrac{\Delta t \Delta z}{2R\varepsilon_0 \Delta x \Delta y}}{1 + \dfrac{\Delta t \Delta z}{2R\varepsilon_0 \Delta x \Delta y}}\right) E_z\Big|_{i,j,k}^{n} + \left(\frac{\dfrac{\Delta t}{\varepsilon_0}}{1 + \dfrac{\Delta t \Delta z}{2R\varepsilon_0 \Delta x \Delta y}}\right)(\nabla \times \boldsymbol{H})_z\Big|_{i,j,k}^{n+1/2} \tag{5.8}$$

To make a capacitance with a capacitor, from the initial equation we obtain this in which we practically remove the losses.

For the parallel combination of a capacitor C and resistor R:

$$E_z\Big|_{i,j,k}^{n+1} = \left(\frac{1 - \dfrac{\Delta t\,\Delta z}{2R\varepsilon_0\,\Delta x\,\Delta y} + \dfrac{C\,\Delta z}{\varepsilon_0\,\Delta x\,\Delta y}}{1 + \dfrac{\Delta t\,\Delta z}{2R\varepsilon_0\,\Delta x\,\Delta y} + \dfrac{C\,\Delta z}{\varepsilon_0\,\Delta x\,\Delta y}}\right) E_z\Big|_{i,j,k}^{n}$$

$$+ \left(\frac{\dfrac{\Delta t}{\varepsilon_0}}{1 + \dfrac{\Delta t\,\Delta z}{2R\varepsilon_0\,\Delta x\,\Delta y} + \dfrac{C\,\Delta z}{\varepsilon_0\,\Delta x\,\Delta y}}\right) (\nabla \times \boldsymbol{H})_z\Big|_{i,j,k}^{n+1/2} \qquad (5.9)$$

To make the inductance, while we managed the others at the constant level, the inductance must be managed considering an equation declared in the code (calculate E inductor), we must do as with the diode, with the advantage that the inductance equation is simpler than to the transcendent of the diode. The summation is made up of all the electric fields at that point.

Regarding evaluating the effectiveness of capacitance, we change capacitance values, raising it we approached the short circuit, to approach the open circuit we needed to lower it.

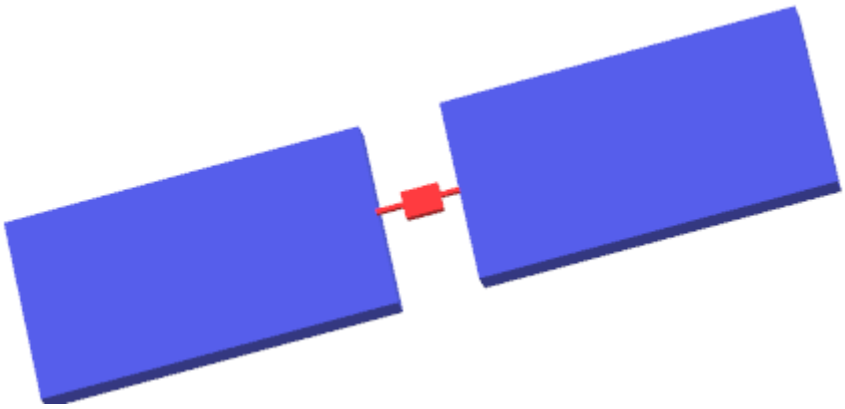

Fig.13: first concept of patch with the capacitance placed in the middle between two microstrips of the trasmission line

Have been processed a series of simulations with various levels of capacitance, then the simulations reveal in V / M the electric field reflected along the Z axis under all

capacitance conditions. The utility of this procedure was to evaluate which kind of values of capacitance we need to use to build the future metasurface.

The repetition of the single metal patch in an organized array is the first approach of building a metasurface.

2.2 BUILDING THE METASURFACE

From this step we proceeded our simulations relying on the use of n Joliot-Curie IRENE-KNL supercomputer in CEA's Very Large Computing Centre (TGCC) in Bruyères-le-Châtel, France. Joliot Curie is a BULL Sequana X1000 supercomputer, funding by Genci, with a peak power of 2 Pflops.

Fig.14: n Joliot-Curie IRENE-KNL supercomputer in CEA's Very Large Computing Centre (TGCC)

The metasurface has been simulated by a set of Perfect Electric Conductor patches connected one to each other through varactor diodes.

From the previous single patch it has been done a repetitive reconstruction of the structure, connected between them by a varactors characterized by the choice of the capacitances evaluated by the previous step on the transmission line.

The first surface model consists of:

- 111 mm x 111 mm surface
- Ground plane/ substrate: No
- 10 x 10 patches
- 1 mm distance between patches
- Dielectric support:

εr: 4.4

σ: 0.0025 S/m

- Varactor diode:

C: 0.1 pF

C: 1 pF

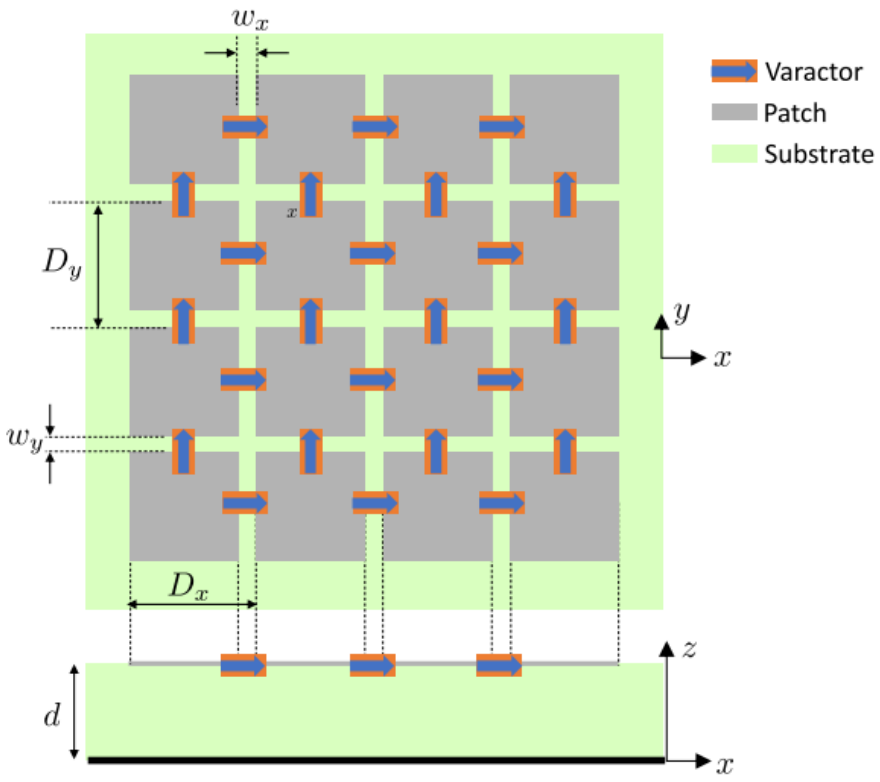

Fig.15 : Geometry of the Reconfigurable Intelligent Surface. Dx , Dy are the periodicity of the lattice and wx and wy are the gaps between the squares patches along x and y planar directions. Varactor diodes connect adjacent cells in both planar directions.

FDTD simulation parameters of :

• Plane incident wave of 1 V/m

• Incident frequency band [1-8] GHz

• Incident angle of

α: 2.8442 Rad

θ:1.6795 Rad

ϕ: 0.5898 Rad

• Detection point located at:

x: 94 ; y: 19 ; z: 2

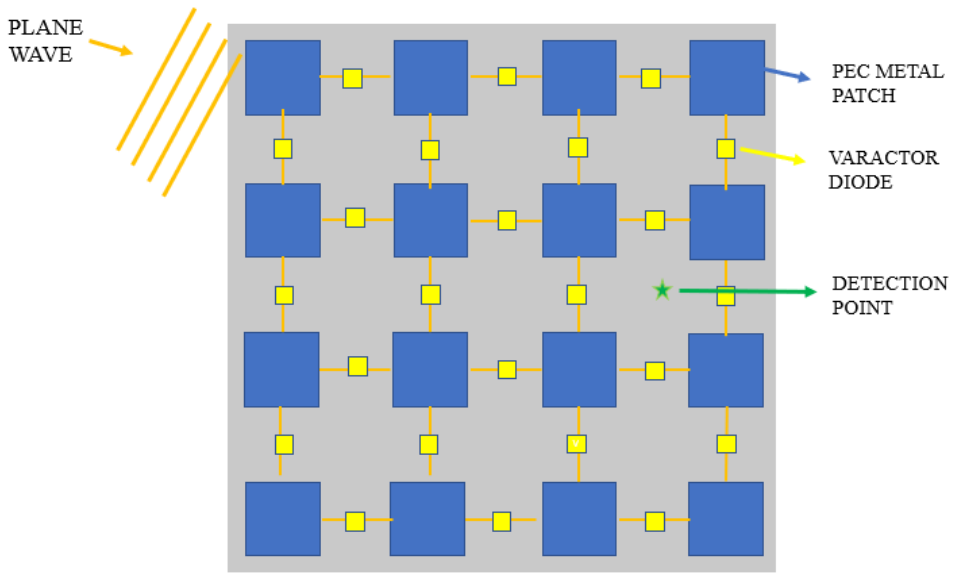

Fig.16: Basic concept of metasurface where is highlighted the point in which the reflected signal is detected

The simulation was based on two step:

• In the first step we transmit a plane EM wave within a frequency band with an arbitrary incident angle to the metasurface

• In the second step we detect the reflected EM wave in an arbitrary point within the working volume in deep near field.

Now we have the first structure of the metasurface, the following steps have the aim to generate a more believable and reliable model of metasurface and to evaluate its functionality in an electromagnetic environment.

- Application of the ground plane to the metasurface: without its presence the impinging wave would pass through the the metasurface and we would not have significant informations from the reflection
- Passing from 10x10 patches to 30x30 patches to gain more informations for the final simulation

- Generating an FDTD environment in which a Biological tissue and a smart device are added

From the simulation done previously we add the ground plane we have done various simulations at different frequencies, then we saw the distribution of the fields on the metasurface and we evaluated the difference between with and without the ground plane. We put on the ground plane because we need the reflection for the final simulation instead without the plane wave would pass through at a different angle.

The 30x30 patches with ground plane simulations of metasurface have been run, we use 0.1 picofarad capacities to test the metasurface and see the electric field distribution on the larger structure by taking min and max points: 6.343 and 6.797 GHz. All this to evaluate the functioning of the metasurface.

2.3 HUMAN BODY MODEL DESIGN

The detailed whole-body virtual model of the human body utilized in the simulation is from the Foundation for Research on Information Technologies in Society's (IT'IS) first generation (V1.0) of virtual models.

A Swiss research foundation called IT'IS builds body models from volunteer participants' magnetic resonance images in order to assess electromagnetic exposure. Virtual family models come in the V1.x, V2.x, V3.x, and V4.x types.

• The V1.x is the first generation of models that is characterized by an high level of detail and accuracy with a spatial resolution of 1.0x1.0x1.0 mm3 .

• V2.x models are a simplified version in which approximately 300 tissues are combined into 22 tissue groups (identical in all the four maps, except for the reproductive system, which is gender-specific). The simplification involves the tissue number, but not the tissue resolution (the whole-body cell count ranges between 3.6 - 7.7 million cells).

• V3.x is the high-resolution generation of human models. Each including more than 300 anatomical features, a re-segmentation at higher resolution (0.5 × 0.5 × 0.5 mm^3) and an enhanced surface processing method. V3.x are static models and so their posture cannot be modified.

• V4.x is based on the V3.x generation of models. They include more than 1000 anatomical features, and the segmentation is performed at an increased resolution (01 x 0.1 x 0.2 mm) allowing for more detail in objects and segmentation of small structures. The higher resolution yields an extended cardiovascular system and a peripheral nerve network (from the cranium and spinal cord to internal organs and major muscles). Muscles, nerves, and blood vessels have been named and meshed as separate objects.

The DVD with the Virtual Family V1.0 includes both the CAD and voxel format compatible with different simulation platforms. For the study simulation, which involves the use of an FDTD algorithm software, only the voxel models (.raw) are required since the CAD files are used to study different exposure configurations using posture simulation platforms. The whole-body human models include four subjects of study: Duke, Ella, Billie and Thelonious

General information	Sex	Type	Age [Years]	Height [m]	Weight [kg]
Thelonious	male	Child	6	1.16	18.6
Billie	female	Pre-teenager	11	1.49	34
Ella	female	young adult	26	1.63	57.3
Duke	male	Young adult	34	1.77	70.2

Fig.17: general informations about human models

A file text including the unique tissue identification number, the spatial resolution of the cells, and the number of the cell in the x, y, and z coordinates that define the total dimensions of the file have been discovered along with the RAW file.

Finally, extra information files can be downloaded from the "tissue properties" portion of the IT'IS website, including an excel file with the thermal and dielectric properties of the different tissues (Table 1), an explanatory notes file, and a database on tissue morphometry.

Tissue	Dielectric Properties													
Name	ε_0	$\Delta\varepsilon_1$	τ_1 (ms)	α_1	$\Delta\varepsilon_2$	τ_2 (ms)	α_2	σ (S/m)	$\Delta\varepsilon_3$	τ_3 (µs)	α_3	$\Delta\varepsilon_4$	τ_4 (ms)	α_4
Adrenal Gland	4	55	7,958	0,1	2500	159,155	0,1	0,5	100000	159,155	0,2	40000000	15,915	0
Air	1	0	0	0	0	0	0	0	0	0	0	0	0	0
Bile	4	66	7,579	0,05	50	1,592	0	1,4	0	159,155	0,2	0	15,915	0,2
Blood	4	56	8,377	0,1	5200	132,629	0,1	0,7	0	159,155	0,2	0	15,915	0
Blood Vessel Wall	4	40	8,842	0,1	50	3,183	0,1	0,25	100000	159,155	0,2	10000000	1,592	0
Bone	2,5	10	13,263	0,2	180	79,577	0,2	0,02	5000	159,155	0,2	100000	15,915	0
Bone (Cancellous)	2,5	18	13,263	0,22	300	79,577	0,25	0,07	20000	159,155	0,2	2000000	15,915	0
Bone (Cortical)	2,5	10	13,263	0,2	180	79,577	0,2	0,02	5000	159,155	0,2	100000	15,915	0
Bone Marrow (Red)	2,5	9	14,469	0,2	80	15,915	0,1	0,1	10000	1591,549	0,1	2000000	15,915	0,1
Bone Marrow (Yellow)	2,5	3	7,958	0,2	25	15,915	0,1	0,0005	5000	1591,549	0,1	2000000	15,915	0,1
Brain	4	40	7,958	0,1	700	15,915	0,15	0,04	200000	106,103	0,22	45000000	5,305	0
Brain (Grey Matter)	4	45	7,958	0,1	400	15,915	0,15	0,02	200000	106,103	0,22	45000000	5,305	0
Brain (White Matter)	4	32	7,958	0,1	100	7,958	0,1	0,02	40000	53,052	0,3	35000000	7,958	0,02
Breast Fat	2,5	3	17,68	0,1	15	63,66	0,1	0,01	50000	454,7	0,1	20000000	13,26	0
Breast Gland	4	55	7,958	0,1	2500	159,155	0,1	0,5	100000	159,155	0,2	40000000	15,915	0
Bronchi	2,5	38	7,958	0,1	400	63,662	0,1	0,3	50000	15,915	0,2	1000000	15,915	0
Bronchi lumen	1	0	0	0	0	0	0	0	0	0	0	0	0	0
Cartilage	4	38	13,263	0,15	2500	144,686	0,15	0,15	100000	318,31	0,1	40000000	15,915	0
Cerebellum	4	40	7,958	0,1	700	15,915	0,15	0,04	200000	106,103	0,22	45000000	5,305	0

Cerebrospinal Fluid	4	65	7,958	0,1	40	1,592	0	2	0	159,155	0	0	15,915	0
Cervix	4	45	7,958	0,1	200	15,915	0,1	0,3	150000	106,103	0,18	40000000	1,592	0
Commissural Anterior	4	32	7,958	0,1	100	7,958	0,1	0,02	40000	53,052	0,3	35000000	7,958	0,02
Commissural Posterior	4	32	7,958	0,1	100	7,958	0,1	0,02	40000	53,052	0,3	35000000	7,958	0,02
Connective Tissue	4	42	12,243	0,1	60	6,366	0,1	0,25	60000	318,31	0,22	20000000	1,326	0
Diaphragm	4	50	7,234	0,1	7000	353,678	0,1	0,2	1200000	318,31	0,1	25000000	2,274	0
Ductus Deferens	4	40	8,842	0,1	50	3,183	0,1	0,25	100000	159,155	0,2	10000000	1,592	0
Dura	4	40	7,958	0,15	200	7,958	0,1	0,5	10000	159,155	0,2	1000000	15,915	0
Epididymis	4	55	7,958	0,1	5000	159,155	0,1	0,4	100000	159,155	0,2	40000000	15,915	0
Esophagus	4	60	7,958	0,1	2000	79,577	0,1	0,5	100000	159,155	0,2	40000000	15,915	0
Esophagus Lumen	1	0	0	0	0	0	0	0	0	0	0	0	0	0
Eye (Cornea)	4	48	7,958	0,1	4000	159,155	0,05	0,4	100000	15,915	0,2	40000000	15,915	0
Eye (Lens)	3	32	8,842	0,1	100	10,61	0,2	0,2	1000	15,915	0,2	5000	15,915	0
Eye (Sclera)	4	50	7,958	0,1	4000	159,155	0,1	0,5	100000	159,155	0,2	5000000	15,915	0
Eye (Vitrous Humor)	4	65	7,234	0	30	159,155	0,1	1,5	0	159,155	0	0	15,915	0
Eye Lens (Cortex)	4	42	7,958	0,1	1500	79,577	0,1	0,3	200000	159,155	0,1	40000000	15,915	0
Eye Lens (Nucleus)	3	32	8,842	0,1	100	10,61	0,2	0,2	1000	15,915	0,2	5000	15,915	0
Fat	380	0	1	380	380	5,89	0,00	1	5,89	5,89	4	50	7,958	0,1
Fat (Average Infiltrated)	0	0	1	0	0	0,00	0,00	1	0,00	0,00	4	65	7,234	0
Fat (Not Infiltrated)	0	0	1	0	0	0,00	0,00	1	0,00	0,00	4	42	7,958	0,1
Gallbladder	0	0	1	0	0	0,00	0,00	1	0,00	0,00	3	32	8,842	0,1
Heart Lumen	33	13	12	20	63	0,51	0,20	12	0,31	0,98	2,5	9	7,958	0,2
Heart Muscle	33	13	12	20	63	0,51	0,20	12	0,31	0,98	2,5	9	7,958	0,2
Hippocampus	0	0	1	0	0	0,00	0,00	1	0,00	0,00	2,5	3	7,958	0,2
Hypophysis	30	0	1	30	30	0,46	0,00	1	0,46	0,46	4	55	7,579	0,05
Hypothalamus	10000	0	1	10000	10000	0,00	0,00	1	0,00	0,00	4	56	8,377	0,1
Intervertebral Disc	1024	310	24	609	1719	39,36	11,92	24	23,42	66,08	4	50	7,958	0,1
Kidney	763	86	3	670	840	15,53	1,75	3	13,63	17,09	4	45	7,958	0,1
Kidney (Cortex)	885	304	2	670	1100	13,71	4,71	2	10,38	17,04	4	55	7,958	0,1
Kidney (Medulla)	885	0	1	885	885	18,01	0,00	1	18,01	18,01	4	55	7,958	0,1
Large Intestine	35	0	1	35	35	0,54	0,00	1	0,54	0,54	4	38	13,263	0,15
Large Intestine Lumen	4161	541	43	2607	5571	19,79	2,57	43	12,40	26,50	4	47	7,958	0,1
Larynx	3953	914	8	2750	5060	18,80	4,35	8	13,08	24,07	4	47	7,958	0,1
Liver	599	191	4	350	770	2,85	0,91	4	1,66	3,66	4	47	7,958	0,1
Lung	765	232	20	335	1236	11,85	3,59	20	5,19	19,14	4	50	7,958	0,1
Lung (Deflated)	0	0	1	0	0	0,00	0,00	1	0,00	0,00	4	50	7,234	0,1
Lung (Inflated)	35	0	1	35	35	0,54	0,00	1	0,54	0,54	4	38	13,263	0,15
Lymphnode	902	228	43	212	1273	10,41	2,63	43	2,45	14,69	4	39	8,842	0,1
Mandible	401	358	8	71	1083	6,21	5,55	8	1,10	16,78	2,5	18	7,958	0,1
Medulla Oblangata	401	358	8	71	1083	6,21	5,55	8	1,10	16,78	4	45	7,958	0,1
Meniscus	401	358	8	71	1083	6,21	5,55	8	1,10	16,78	2,5	18	7,958	0,1
Midbrain	453	49	3	402	500	7,01	0,76	3	6,23	7,74	4	55	7,958	0,1
Mucous Membrane	10	0	1	10	10	0,15	0,00	1	0,15	0,15	2,5	10	13,263	0,2
Muscle	559	99	43	412	976	11,37	2,01	43	8,37	19,87	4	40	7,958	0,1
Nerve	35	0	1	35	35	0,54	0,00	1	0,54	0,54	4	38	13,263	0,15
Ovary	559	99	43	412	976	11,37	2,01	43	8,37	19,87	4	40	7,958	0,1
Pancreas	594	497	3	270	1166	9,19	7,70	3	4,18	18,06	4	39	7,958	0,1
Patella	39	13	43	19	94	0,96	0,32	43	0,46	2,32	4	50	7,234	0,1

Penis	160	30	3	130	189	2,48	0,46	3	2,01	2,93	4	26	7,958	0,1
Pharynx	236	0	1	236	236	3,65	0,00	1	3,65	3,65	4	40	8,842	0,15
Pineal Body	767	357	13	469	1640	11,89	5,53	13	7,26	25,40	4	55	7,958	0,1
Placenta	10	0	1	10	10	0,15	0,00	1	0,15	0,15	2,5	10	13,263	0,2
Pons	12	5	3	7	16	0,19	0,07	3	0,11	0,25	4	40	8,842	0,1
Prostate	0	0	1	0	0	0,00	0,00	1	0,00	0,00	1	0	0	0
Salivary Gland	885	304	2	670	1100	13,71	4,71	2	10,38	17,04	4	55	7,958	0,1
SAT (Subcutaneous Fat)	1700	423	3	1250	2090	26,33	6,55	3	19,36	32,37	4	56	8,377	0,1
Seminal vesicle	559	99	43	412	976	11,37	2,01	43	8,37	19,87	4	40	7,958	0,1
Skin	394	0	1	394	394	6,10	0,00	1	6,10	6,10	4	55	7,958	0,1
Skull	383	10	3	378	394	5,93	0,15	3	5,85	6,10	4	55	7,958	0,1
Small Intestine	33	13	12	20	63	0,51	0,20	12	0,31	0,98	2,5	9	7,958	0,2
Small Intestine Lumen	394	0	1	394	394	6,10	0,00	1	6,10	6,10	4	55	7,958	0,1
Spinal Cord	106	37	12	49	175	1,65	0,57	12	0,76	2,70	4	32	7,234	0
Spleen	10	0	1	10	10	0,15	0,00	1	0,15	0,15	2,5	10	13,263	0,2
Stomach	1026	337	11	560	1528	15,89	5,21	11	8,67	23,67	4	50	7,958	0,1
Stomach Lumen	0	0	1	0	0	0,00	0,00	1	0,00	0,00	4	50	7,234	0,1
Tendon\Ligament	160	30	3	130	189	2,48	0,46	3	2,01	2,93	4	26	7,958	0,1
Testis	1557	723	14	931	3600	24,11	11,20	14	14,41	55,75	4	48	7,958	0,1
Thalamus	460	256	8	106	882	7,13	3,96	8	1,64	13,65	4	60	7,958	0,1
Thymus	0	0	1	0	0	0,00	0,00	1	0,00	0,00	4	50	7,234	0,1
Thyroid Gland	29	0	2	29	29	0,45	0,00	2	0,45	0,45	4	42	12,243	0,1
Tongue	200	24	3	186	228	3,09	0,38	3	2,88	3,53	4	55	7,958	0,1
Tooth	685	289	2	480	889	13,93	5,88	2	9,77	18,09	4	45	7,958	0,1
Tooth (Dentine)	243	0	1	243	243	3,76	0,00	1	3,76	3,76	4	55	7,958	0,1
Tooth (Enamel)	5624	1403	7	3350	7370	87,10	21,73	7	51,88	114,14	4	55	7,958	0,1
Trachea	78	0	1	78	78	1,21	0,00	1	1,21	1,21	4	50	7,958	0,1
Trachea Lumen	0	0	1	0	0	0,00	0,00	1	0,00	0,00	2,5	10	13,263	0,2
Ureter\Urethra	0	0	1	0	0	0,00	0,00	1	0,00	0,00	2,5	10	13,263	0,2
Urinary Bladder	0	0	1	0	0	0,00	0,00	1	0,00	0,00	2,5	10	13,263	0,2
Urinary Bladder Wall	35	0	1	35	35	0,54	0,00	1	0,54	0,54	2,5	38	7,958	0,1
Uterus	0	0	1	0	0	0,00	0,00	1	0,00	0,00	1	0	0	0
Vagina	188	0	1	188	188	2,91	0,00	1	2,91	2,91	4	40	8,842	0,1
Vertebrae	39	0	1	39	39	0,60	0,00	1	0,60	0,60	2,5	16	8,842	0,1

2.4 FINAL SIMULATION SETUP

Fig.18: Dipole antenna, Telonious head model, RIS, smart device and PEC metal barrier disposition for last simulation setup

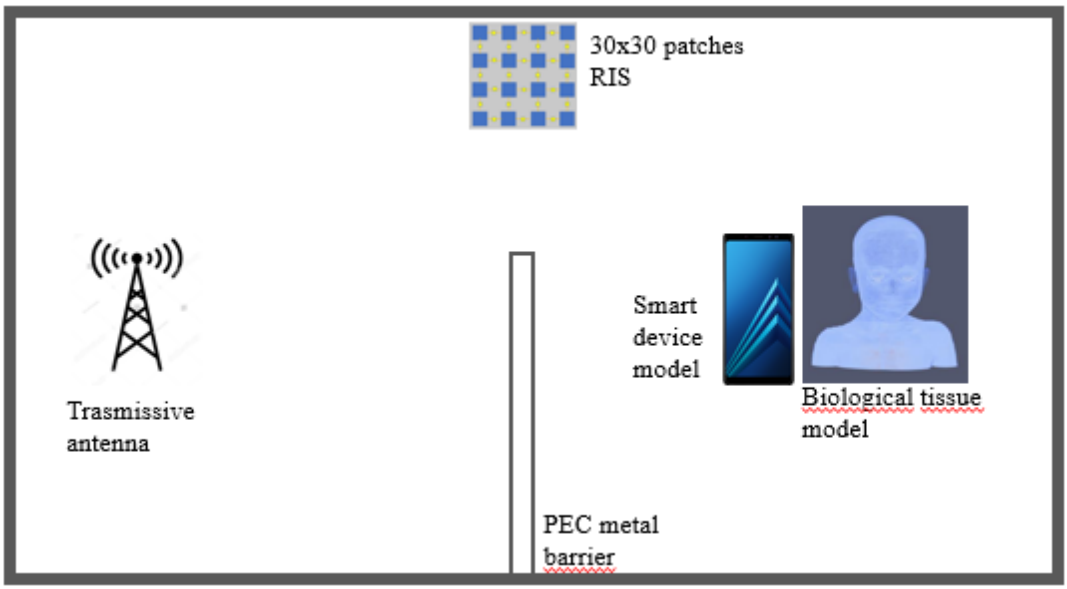

- Environment dominium: 600x600x500 cells
- 1 mm cells
- Thelonious head placement:
- Smart device placement:
- Metasurface placement:
- Antenna placement:
- PEC metal barrier placement:

- METASURFACE CONSIDERED

  311 mm x 311 mm surface

  10 x 10 patches

  Ground plane/ substrate: YES

  1 mm distance between patches

  Dielectric support: εr: 4.4 and σ: 0.0025 S/m

  Varactor diode: C: 0.1 pF and C: 1 pF

  The use of a bigger metasurface allows to reproduce more reliable results.

- SMART DEVICE MODEL

  It is considered as an antenna of dimensions: 1x20x9 cells.

  The dimensions have been decided to simulate the mobile phone antenna

- TISSUE CONSIDERED

  Thelonious head dimensions: 403x225x300 cells.

  The final simulation had been processed just by the use of Thelonious head body map.

  To visualize the model in a 3D space, the ParaView software has been used. ParaView is an open-source, multi-platform data analysis application for interactive, scientific visualization, released in 2002 by Kitware software company. This application is suitable for different kinds of simulations, from academic to research purposes and it's characterized by an intuitive and compact design user interface where all the important tools are located in the main window.

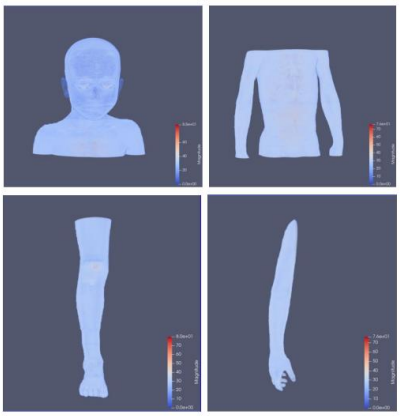

- ANTENNA CHARACTERISTICS

  Dipole Antenna dimensions: 1x1x λ/2.

  The simulation analysis of the presented antenna is carried out through FDTD technique, implemented with C programming language.

  A dipole antenna is an antenna with a center-fed driven element for transmitting or receiving radio frequency energy. From a physics viewpoint, this type of antenna is the simplest practical antenna. It consists of a straight electric conductor, made of conducting metal such as copper, interrupted at the center, therefore making two poles.

- PEC METAL BARRIER

  Dimensions 1x350x350.

  A perfect conductor or perfect electric conductor (PEC) is an idealized material exhibiting infinite electrical conductivity or, equivalently, zero resistivity (cf. perfect dielectric). While perfect electrical conductors do not exist in nature, the concept is a useful model when electrical resistance is negligible compared to other effects. One example is ideal magnetohydrodynamics, the study of perfectly conductive fluids. Another example is electrical circuit diagrams, which carry the implicit assumption that the wires connecting the components have no resistance. Yet another example is in computational electromagnetics, where PEC can be simulated faster, since the parts of equations that take finite conductivity into account can be neglected.

3 RESULTS

3.1 CAPACITANCE FOR VARACTOR EVALUATION

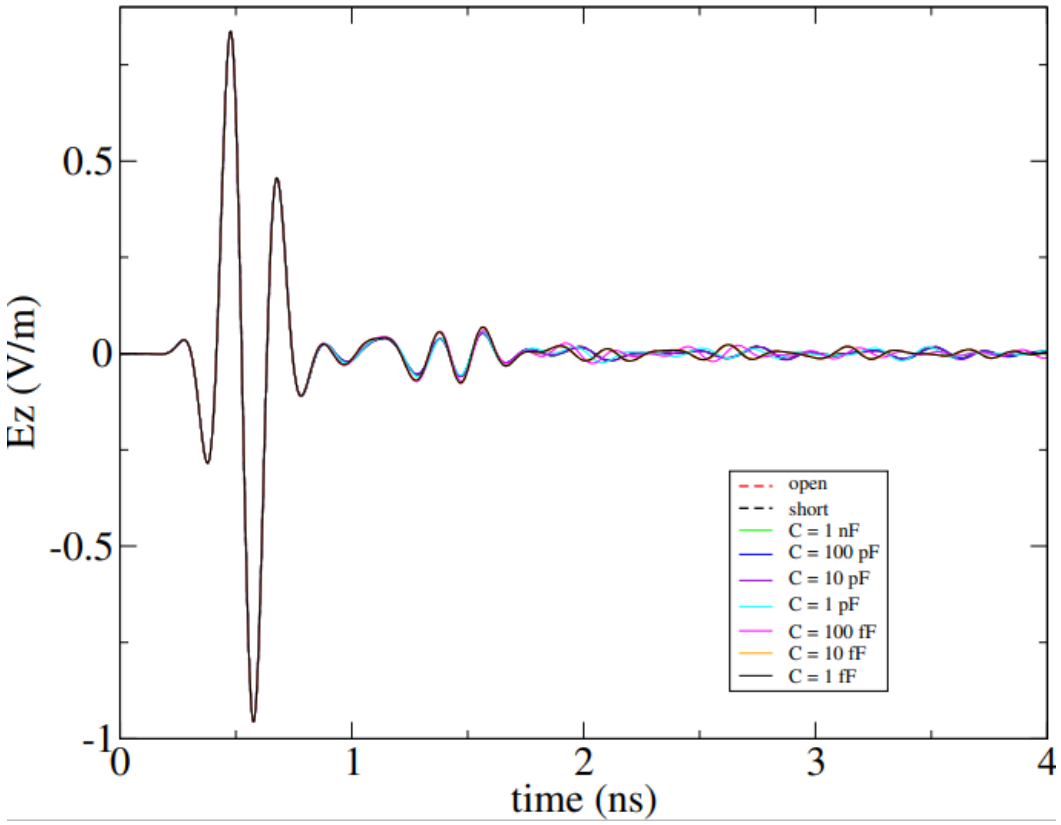

Fig.19 : Electric field reflected along the z axes of the trasmission line with a series of different capacitances placed in the centre

The simulation reveals in V / M the electric field reflected along the Z axis under all capacitance conditions.

It is possible to see how in the case of two microstrips joined with pec metal the result is as if it were a short circuit: we have seen that for certain values of the capacitor, the simulation of the capacitor and single strip (short) are very similar, an expected result

because at 1 nanofarad are values close to the short circuit. We hypothesize that for increasing values of the capacity we should get closer to the short circuit. This helps us to understand what values to give to the capacitances for the final metasurface model.

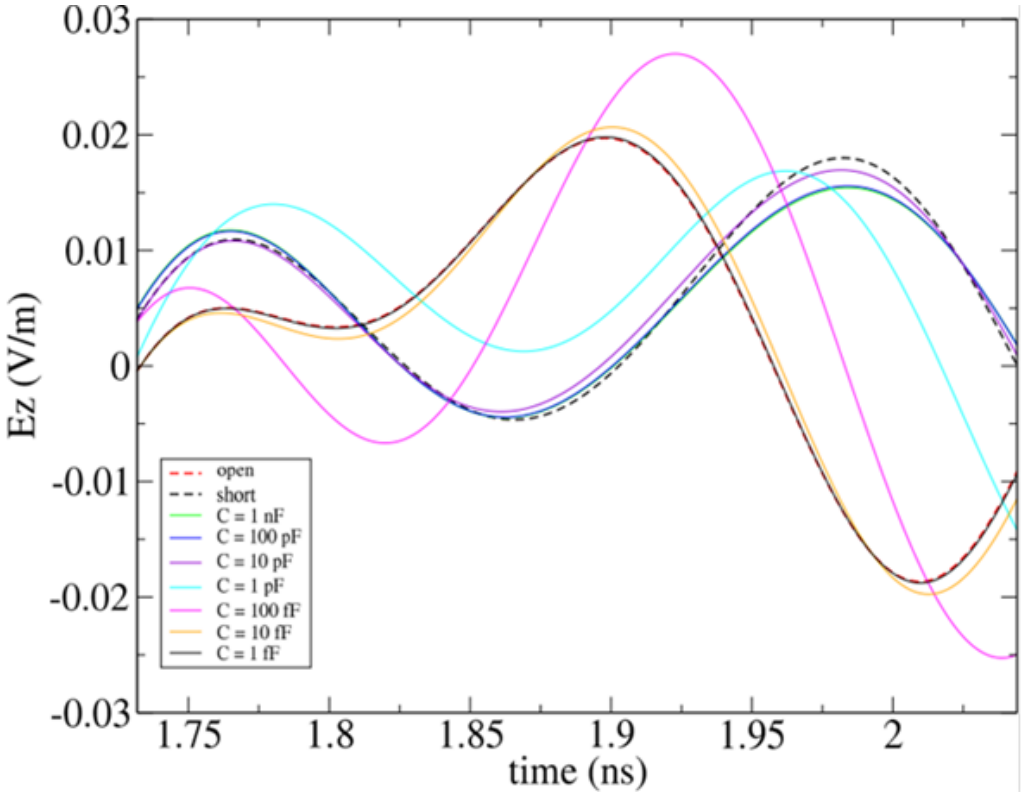

Fig.20 : third reflection along the z axes of the trasmission line

As it is possible to see, the direct impulse from the board comes first, then the reflections.

The reflections from the line are the ones that see the polarization of the diode

The impulse arrives at a point and this is the component along z, the first signal that arrives is the direct wave which is the same for all capacitance values, the first reflection is always almost the same or in any case very similar. it can be seen that up to one nanosecond only direct wave is present.

From 1 to 1.5 is 1 reflection due to the whole ground plane, in which few differences are deduced, subsequently

From the 3rd reflection onwards there are differences based on the capacitance, the differences are due to the polarization and we see that for high values up to 1 nanofarad we get close to the short circuit, dropping the values up to 1 femtofarad we get up to above the circuit open.

After these simulations capacitances with 1picoFarad and with 0.1 picoFarad had been chosen for the following simulations, due to the fact that these two capacitances are the ones which get closer to short and open circuit.

3.2 10X10 METASURFACE RECEIVED SIGNAL

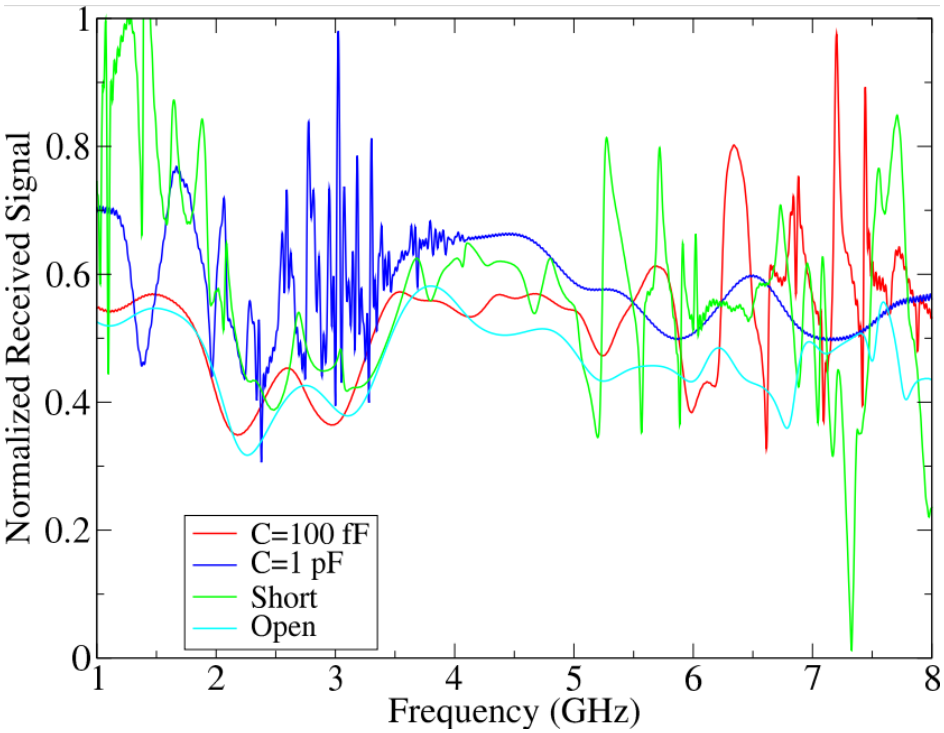

Fig 21.: Normalized received signal in an arbitrary point from a 10x10 metasurface at different varactor capacitances

The received signals from the first concept of metasurface, evaluated at the detection point.

Here is possible to see the comparison between the two capacitances, the short circuit (PEC metal microstrip in the place of the capacitance) and the open circuit (no element between patches).

FDTD simulation method allow us to pass from time-domain signals to frequency-domain signals by the use of Fast Fourier Trasform.

Had been chosen [1-8] GHz band because is a believable 5G band that well fits to our FDTD domain

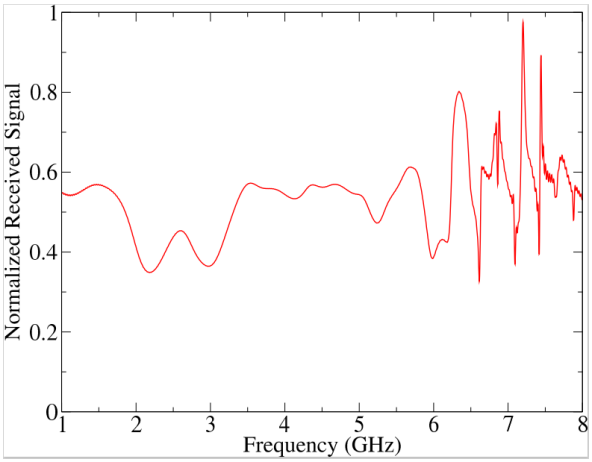

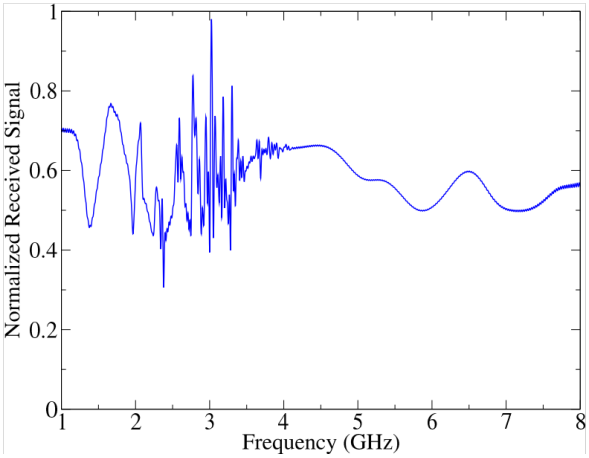

- In the case of 0.1 picoFarad the detection point shows a minus peak f1 at 2.2 GHz and a maximum peak f2 at 6.4 GHz after which shows more irregular oscillations
- In the case of 1 picoFarad the detection point shows a a minus peak f3 at 2.4 GHz and a maximum peak f4 at 3.1 GHz on 0-6 GHz frequency band

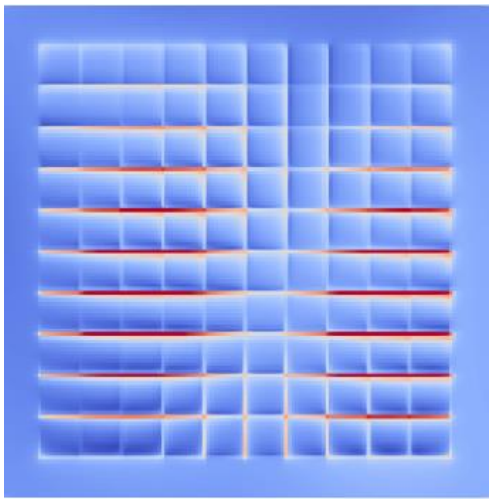

Fig. 22 : Electric field distribution on metasurface at f1 frequency, 0.1picoFarad capacitance.

Electric field distribution on metasurface at f1 frequency, 0.1 picoFarad capacitance.

Distribution of the magnitude of the electric field on the metasurface at the frequency f1 where a min peak was shown in the detected signal.

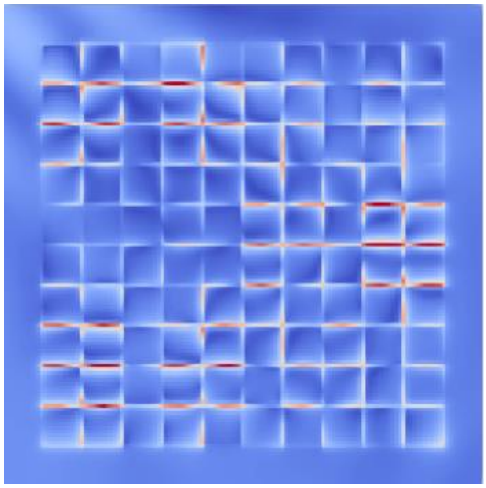

Fig. 23 : Electric field distribution on metasurface at f2 frequency, 0.1picoFarad capacitance.

Electric field distribution on metasurface at f2 frequency, 0.1 picoFarad capacitance.

Distribution of the magnitude of the electric field on the metasurface at the frequency f2 where a max peak was shown in the detected signal.

- To be noted that the maximum values of the electric field are more spotted on the surface

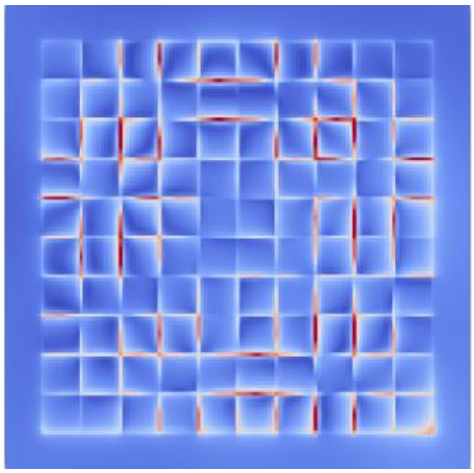

Fig. 24 : Electric field distribution on metasurface at f3 frequency, 1picoFarad capacitance.

Electric field distribution on metasurface at f3 frequency, 1picoFarad capacitance.

Distribution of the magnitude of the electric field on the metasurface at the frequency f3 where a min peak was shown in the detected signal.

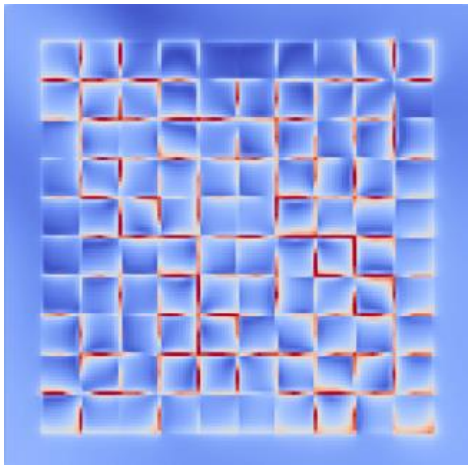

Fig.25 : Electric field distribution on metasurface at f4 frequency, 1picoFarad capacitance.

Electric field distribution on metasurface at f4 frequency, 1 picoFarad capacitance.

Distribution of the magnitude of the electric field on the metasurface at the frequency f4 where a max peak was shown in the detected signal.

- To be noted that the maximum values of the electric field are distributed irregularly on the surface
- These previous electric field distributions on the Metasurface provide an useful information because these distributions are not constant or homogeneous, so this means that are dependent by the interaction of the incident wave, the diode state, and the incident angle, so if it is possible having a distribution dependent on diode configuration we could work reversely, so providing a precise diode configuration with the aim to have a precise electric field distribution on the surface.

- The electric field distributions are registered 1 mm up from the surface, not directly on the surface.

- Is important to see how the Electric field distribution varies in base on the change of the diodes configuration, so we could understand which is the right diode configuration to have the desired E.F. distribution

- The successive step will be done thanks to optimization algorithms, in which will be possible to define which must be the best diode configuration that corresponds to the desired reflected beam focalization, and this focalization should be done automatically instead of manually.

3.3 GROUND PLANE 10X10 RIS RECEIVED SIGNAL

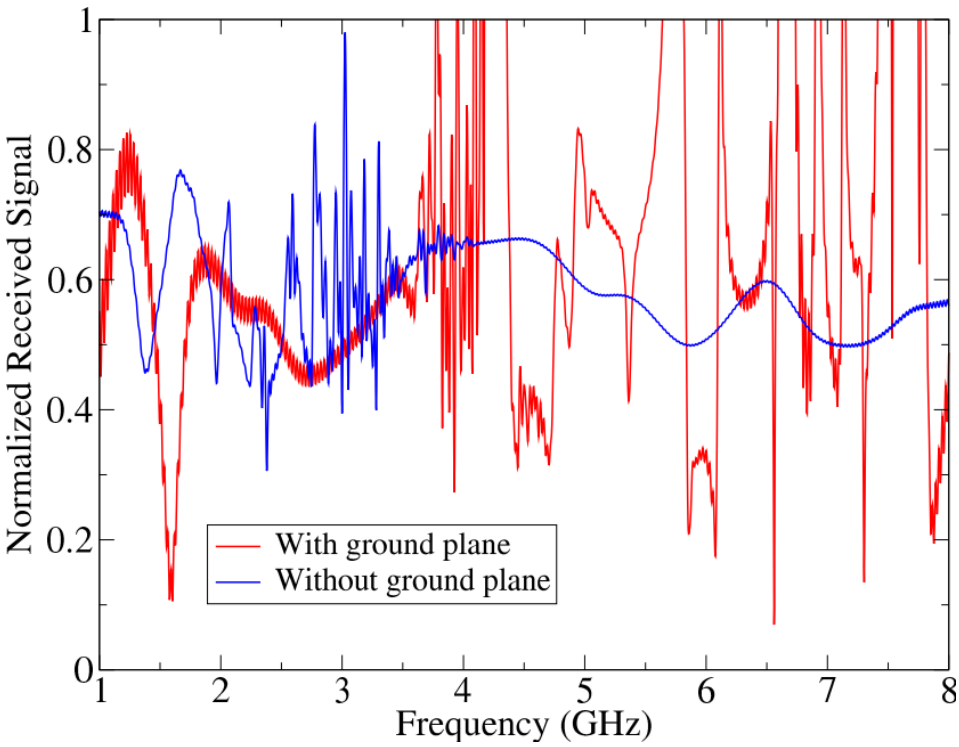

Fig.26 : The simulation without ground plane at 1picoFarad is put in comparison with the one at the same capacitance with the application of the ground plane, at the same detection point

The simulation without ground plane at 1picoFarad is put in comparison with the one at the same capacitance with the application of the ground plane, at the same detection point.

3.4 GROUND PLANE 30X30 RIS RECEIVED SIGNAL

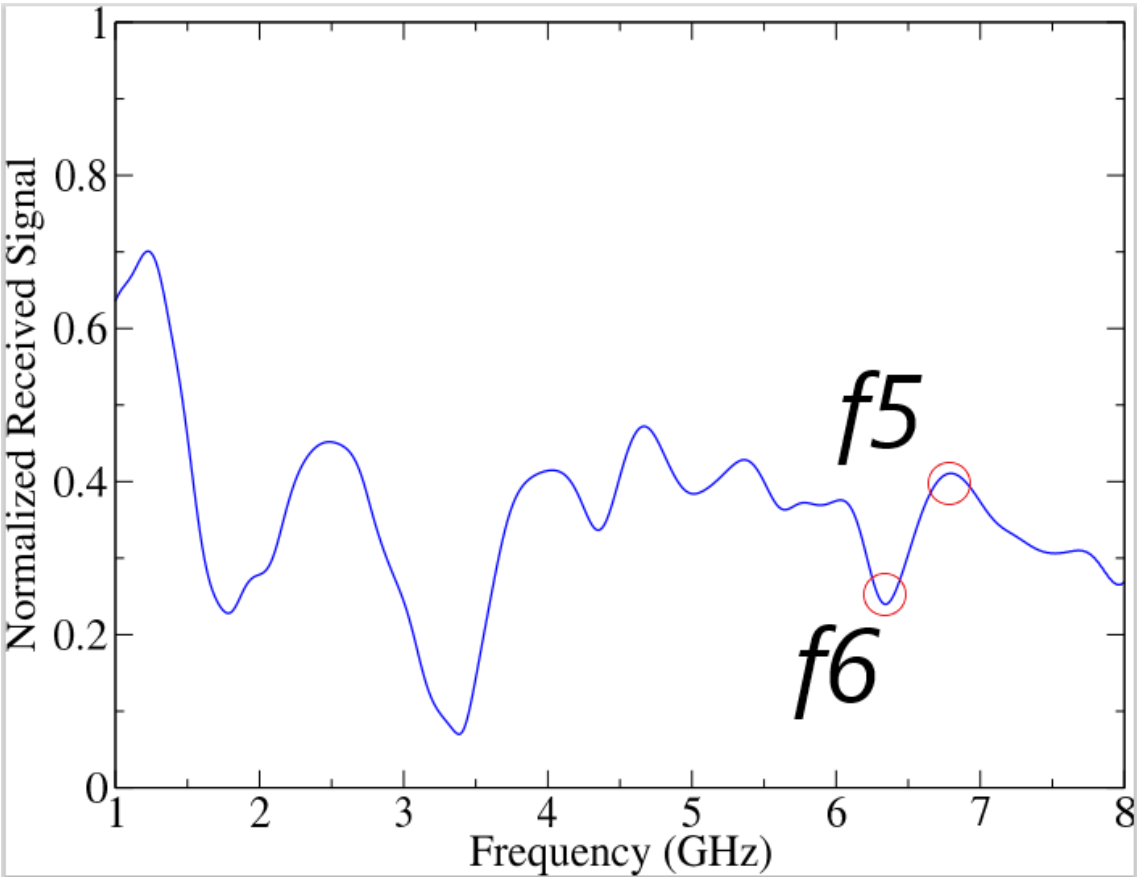

Fig.27 : The received signal from the detection point of the 30x30 patches metasurface

The received signal from the detection point of the 30x30 patches metasurface, then to evaluate the electric field distribution on the surface it had been taken the minimum and maximum points at 6.343 and 6.797 GHz, respectively.

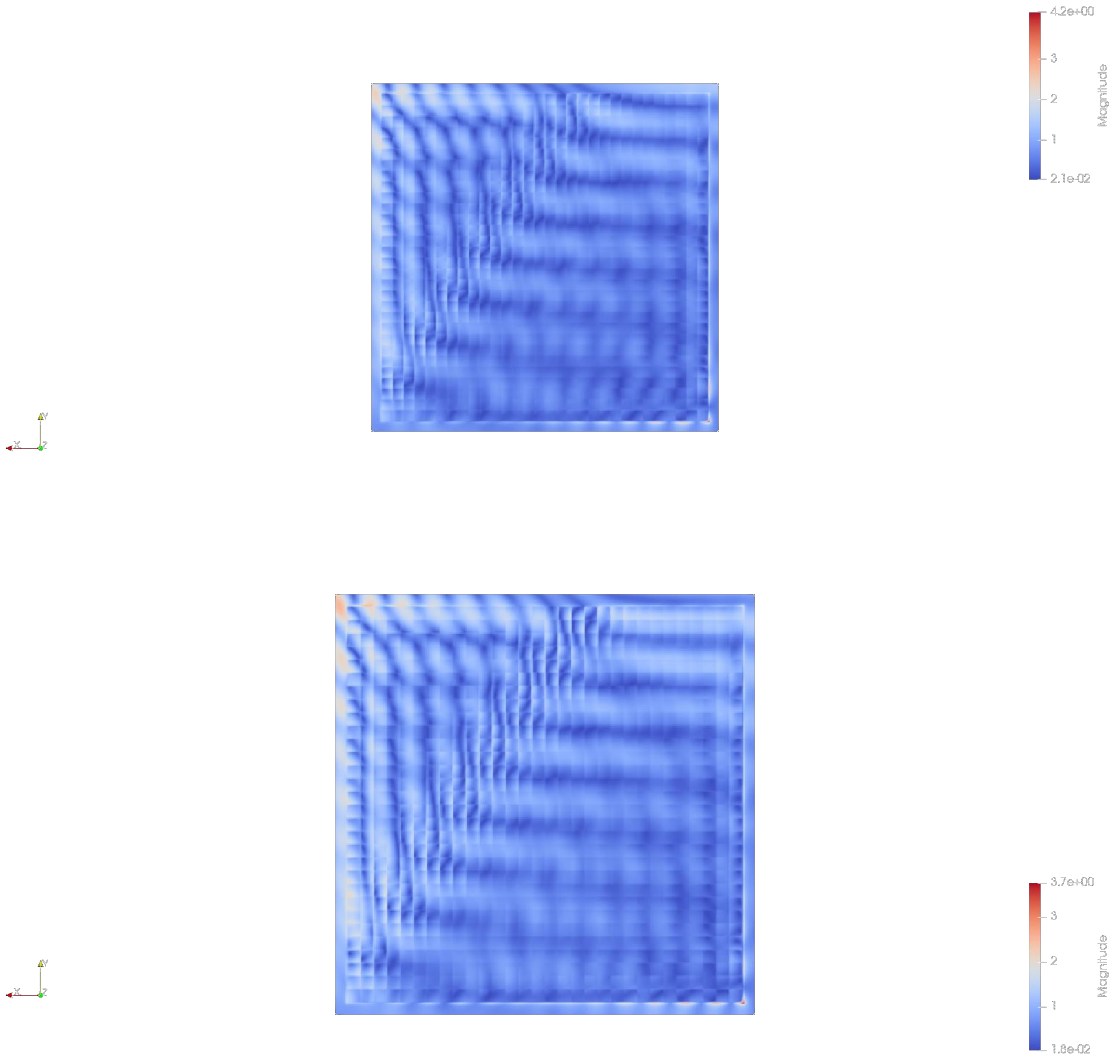

In this phase we wanted to test the metasurface and see the distribution of the electric field on the larger structure, using a capacity of 0.1 picoFarad, and these are the pictures taken from a 30x30 patches and so 311x311 mm metasurface in the minimum and maximum points f5 and f6 from the previous signal.

4. DISCUSSIONS AND CONCLUSIONS

What we are able to see and from what the previous results showed us we were able to develop and simulate through the FDTD simulation method implemented with the C language a manually reconfigurable metasurface and evaluate the electric field distributions along it following the emission of a plane wave, and it was also possible to evaluate the reflection of this wave at an arbitrary point in the FDTD space lattice.

It could be shown that different diode configurations cause different reflections of the the plane wave passing through the metasurface so the possibility of giving a certain configuration in terms of capacitance to the varactor diodes in such a way that a desired focus of the reflected signal can be had.

Regarding the last simulation the objective was to show that with the use of a meta-surface in an open environment causes a better focusing of the signal sent by the dipole antenna and thus a better focusing of the signal on the device instead of on the biological tissues of the human body, in this case the Thelonious's head. In fact, the first simulation that was done did not include the metasurface but simply an environment consisting of an obstacle, dipole antenna, human body and device, then Thelonious head SAR was evaluated. After that, an attempt was made to insert the metasurface and generate a configuration in the varactor diodes such that the reflected signal may have focused in the direction of the device and in turn we tried to prove that the metasurface is capable of giving a precise directionality in a given position by limiting the electromagnetic exposure of the tissues by focusing the radiofrequency wave on the device rather than on the human body.

BIBLIOGRAPHY

[1] I Metamateriali: Invisibilità e Rifrazione Negativa in Mezzi Nanochirali Marco Esposito Dipartimento di Matematica & Fisica “Ennio De Giorgi” - Università del Salento, CNR Nanotec Francesco Todisco Dipartimento di Matematica & Fisica “Ennio De Giorgi” - Università del Salento, CNR Nanote.

[2] Wireless Communications Through Reconfigurable Intelligent Surfaces ERTUGRUL BASAR 1 (Senior Member, IEEE), MARCO DI RENZO2 , (Senior Member, IEEE), JULIEN DE ROSNY3 , MEROUANE DEBBAH4,5, (Fellow, IEEE), MOHAMED-SLIM ALOUINI 6 , (Fellow, IEEE), AND RUI ZHANG 7 , (Fellow, IEEE)

[3] FD-TD Modeling of Digital Signal Propagation in 3-D Circuits With Passive and Active Loads Melinda Piket-May, Member. IEEE, Allen Taflove, Fellow, IEEE, and John Baron, Student Member, IEEE

[4] Generalized Sheet Transition Condition FDTD Simulation of Metasurface Yousef Vahabzadeh , Nima Chamanara , and Christophe Caloz, Fellow, IEEE

[5] Simultaneous Control of the Spatial and Temporal Spectra of Light With Space-Time Varying Metasurfaces Nima Chamanara , Yousef Vahabzadeh, Student Member, IEEE, and Christophe Caloz , Fellow, IEEE

[6] Computationai Electrodynamics The Finite-Difference Time-Domain Method Third Edition Allen Taflove Susan C. Hagness

[7] K. S. Kunz and R. J. Luebbers, “The Finite Difference Time Domain Method for Electromagnetics,” The Finite Difference Time Domain Method for Electromagnetics. 2018.

[8] J. Reddy, “Solutions manual for An introduction to the finite element method,” Essentials Finite Elem. Method, p. 41, 2006.

[9] K. S. Yee, “Numerical Solution of Initial Boundary Value Problems Involving Maxwell’s Equations in Isotropic Media,” IEEE Trans. Antennas Propag., vol. 14, no. 3, pp. 302–307, 1966.

[10] A. Taflove, “Application of the Finite-Difference Time-Domain Method to Sinusoidal Steady-State Electromagnetic-Penetration Problems,” IEEE Trans. Electromagn. Compat., vol. EMC-22, no. 3, pp. 191–202, 1980.

[11] J. B. Schneider, “Understanding the Finite-Difference Time-Domain Method,” 2021.

[12] A. Taflove and S. C. Hagness, The Finite-Difference Time-Domain Method Third Edition.

[13] M. Stabin, “Nuclear medicine dosimetry,” Phys. Med. Biol., vol. 51, no. 13, 2006.

[14] J. Wiart, A. Hadjem, M. F. Wong, and I. Bloch, “Analysis of RF exposure in the head tissues of children and adults,” Phys. Med. Biol., vol. 53, no. 13, pp. 3681–3695, 2008.

[15] I. G. Zubal, C. R. Harrell, E. O. Smith, Z. Rattner, and G. Gindi, “Computerized three dimensional segmented human anatomy,” Med. Phys., vol. 21, no. 2, pp. 299–302, 1994.

[16] J. Sühnel and H. Berg, Biological Effects of Electromagnetic Fields (Mechanisms, Modeling, Biological Effects, Therapeutic Effects, International Standards, Exposure Criteria), vol. 61, no. 1–2. 2003

[17] R. Habash, “Biological effects of electromagnetic fields,” Eng. Electromagn. Appl., vol. 416, pp. 189–210, 2006.

[18] K. B. Baker et al., “Evaluation of specific absorption rate as a dosimeter of MRI-related implant heating,” J. Magn. Reson. Imaging, vol. 20, no. 2, pp. 315–320, 2004.

[19] C. K. Chou et al., “Radio frequency electromagnetic exposure: Tutorial review on experimental dosimetry,” Bioelectromagnetics, vol. 17, no. 3, pp. 195–208, 1996.

[20] K. Guido and A. Kiourti, “Wireless Wearables and Implants: A Dosimetry Review,” Bioelectromagnetics, vol. 41, no. 1, pp. 3–20, 2020

[21] Electromagnetic Model of Reflective Intelligent Surfaces FILIPPO COSTA 1 (Senior Member, IEEE), AND MICHELE BORGESE2 (Member, IEEE) 1Dipartimento di Ingegneria dell’Informazione, University of Pisa, 56122 Pisa, Italy

[22] https://greenerwave.com/.